Spring 1-1-2016

Characterizing and Modeling Hydroclimate Extremes in the Western US

Cameron W. Bracken
University of Colorado at Boulder, cameron.bracken@gmail.com

Characterizing and modeling hydroclimate extremes in the Western US

by

C. W. Bracken

B.S., Humboldt State University, 2009

M.S., University of Colorado at Boulder, 2011

A thesis submitted to the

Faculty of the Graduate School of the

University of Colorado in partial fulfillment

of the requirements for the degree of

Doctor of Philosophy

Department of Civil, Environmental and Architectural Engineering

2016

This thesis entitled:
Characterizing and modeling hydroclimate extremes in the Western US
written by C. W. Bracken
has been approved for the Department of Civil, Environmental and Architectural Engineering

_____
Prof. Balaji Rajagopalan

_____
Dr. Subhrendu Gangopadhyay

_____
Prof. William Kleiber

_____
Prof. Ben Livneh

_____
Prof. Joseph Kaspryzk

Date _____

The final copy of this thesis has been examined by the signatories, and we find that both the content and the form meet acceptable presentation standards of scholarly work in the above mentioned discipline.

Bracken, C. W. (Ph.D., Civil Engineering)

Characterizing and modeling hydroclimate extremes in the Western US

Thesis directed by Prof. Balaji Rajagopalan

In the semi-arid western US, water resources infrastructure such as dams, levies, and canals provide a reliable water supply, flood mitigation, and hydropower generation. The ability to manage these aging infrastructure efficiently for hydroclimate extremes such as floods, in a nonstationary climate, is crucial for the sustainability of the region. Traditional methods for analyzing hydroclimate extremes assume stationarity of climate in space and time and do not capture uncertainty in a robust manner, leading to inaccurate estimation and misrepresentation of risk.

This dissertation is motivated by the need for a mechanistic understanding of hydroclimate extremes and a general framework to model them across the entire western US, while maintaining a robust quantification of uncertainty. To this end, this dissertation makes four contributions: (1) Identification of eight seasonally dependent and spatially coherent regions for precipitation extremes in the western US and the dominant moisture sources and delivery pathways for each region. Extreme value clustering and storm trajectory analysis were used in this effort. (2) Development of a Bayesian hierarchical spatial model for precipitation extremes in large regions, such as the western US, incorporating data from thousands of observation locations. This model can produce maps of gridded return levels and to simulate gridded precipitation extremes at any resolution, with associated uncertainties. (3) Development of a Bayesian hierarchical model for joint nonstationary precipitation and streamflow frequency analysis in rainfall-runoff dominated basins such as those in the southwest US. Peak streamflow is modeled as a consequence of spatial precipitation extremes, allowing for temporal nonstationarity from climate covariates. (4) Development of a general hierarchical Bayesian multivariate nonstationary frequency analysis framework with an application to dam safety analysis. In this, the peak snow depth and peak streamflow are linked to reservoir water level and, consequently, dam safety. These contributions pro-

vide new insights into the mechanisms influencing hydroclimate extremes in the western US and offer new frameworks for spatial, nonstationary, and multivariate modeling of extremes with an emphasis on the robust quantification of uncertainties. These contributions have significant applicability to engineering design, planning, risk assessment, and mitigation strategies for managing aging infrastructure under changing climate hazards.

Dedication

To my Dad.

Acknowledgements

Contents

Chapter

Tables

Table

Figures

Preface

This dissertation organized in article format. Each chapter is written as a standalone article for journal submission. As such, each chapter contains standalone introductions as well as conclusions. An aggregated bibliography has been provided for the entire dissertation following Chapter 4 due to many overlapping references.

Overview

Extreme hydroclimate events are rare by definition but have a disproportionate effect on infrastructure, the environment, the economy and human life. The incorporation of extreme value analysis has long been standard practice in civil engineering design and management dating back to [*Gumbel*, 1941]. The typical goal of an extreme value analysis is the estimation of a return level, or the magnitude of an extreme event associated with a given return period. While the motivation to provide better estimates of return levels is self-evident, engineering practice remains somewhat rudimentary despite substantial research improvements in recent years [*Katz et al.*, 2002]. The assumptions of traditional extreme value analysis are adequately summarized by Gumbel:

> "In order to apply any theory we have to suppose that the data are homogeneous, i.e. that no systematical change of climate and no important change in the basin have occurred within the observation period and that no such changes will take place in the period for which extrapolations are made." [*Gumbel*, 1941]

Analysis of hydroclimate extremes began as a single site procedure and surprisingly remains the recommended procedure for determining flood frequency estimates for a basin [*USGS*, 1981]. This approach has some obvious drawbacks; namely, it ignores any spatial coherence that may be present across multiple sites and it cannot be applied to sites with no observations. Regional frequency analysis (RFA) is a popular methodology that addresses both issues [*Hosking et al.*, 1985]. RFA aims to improve frequency estimates at all sites in a homogeneous region and enables the transfer of frequency estimates to ungaged sites. The probability weighted moments (PWM) or "L-moments" approach is a common component of RFA because of its speed of computation and good performance with small samples [*Katz et al.*, 2002]. While RFA provides obvious advantages

over at-site analyses, it still requires the (often subjective) delineation of homogeneous regions, and traditional implementations do not have the ability to incorporate climate information.

In the western US, there is clear evidence for spatial and temporal nonstationarity in hydro-climate extremes and links to large scale climate [*Arriaga Ramírez and Cavazos*, 2010; *Balling Jr and Goodrich*, 2011; *Cayan et al.*, 2010, 1999; **?**; *Dulière et al.*, 2013b; *Gershunov and Barnett*, 1998; *Higgins et al.*, 2010; *Kunkel*, 2003b, a; *Palecki et al.*, 2005; *Pryor et al.*, 2009; *Schumacher and Johnson*, 2010]. Despite an increasing understanding of how extremes behave historically in space and time, tools to incorporate this information are not widespread. In particular, there is a need for tools which provide seasonal and nonstationary estimates of risk throughout the western US at a scale that is useful for decision making. It is also crucial that these tools provide robust quantifications of uncertainty in return level estimates.

Return levels are traditionally viewed as fixed quantities, though in reality return level estimates have their own probability distributions. Robust quantification of uncertainty is a fundamental component of any frequency analysis. Bayesian model fitting methods provide an avenue to represent the full uncertainty associated with return levels given the data. In recent years Bayesian approaches to modeling extremes have seen an explosion in the literature [*Cooley et al.*, 2007; *Cooley and Sain*, 2010; *Aryal et al.*, 2010; *Atyeo and Walshaw*, 2012; *Davison et al.*, 2012; *Ghosh and Mallick*, 2011; *Reich and Shaby*, 2012; *Sang and Gelfand*, 2010, 2009a; *Apputhurai and Stephenson*, 2013; *Dyrrdal et al.*, 2014]. Chapters 2-4 will utilize Bayesian model fitting procedures in order to quantify the uncertainty in return level estimates.

This dissertation is motivated by the need for a mechanistic understanding of hydroclimate extremes and a general framework to model them across the entire western US, while maintaining a robust quantification of uncertainty. In it, we discusses methods to analyze and model seasonal, spatial, nonstationary and hydroclimate extremes in the western US with an emphasis on the quantification of uncertainty.

Chapter 1 describes a comprehensive analysis of the seasonal spatial behavior of extreme precipitation in the western US. In it, we identify eight seasonally dependent and spatially coher-

ent regions for precipitation extremes in the western US and the dominant moisture sources and delivery pathways for each region. Extreme value clustering and storm trajectory analysis were used in this effort. This chapter sets the stage for the remainder of the thesis providing a physical justification for extreme precipitation and motivation for further statistical work.

Chapter 2 describes the development of a Bayesian hierarchical spatial model for precipitation extremes in large regions, such as the western US, incorporating data from thousands of observation locations. This model can produce maps of gridded return levels and to simulate gridded precipitation extremes at any resolution, with associated uncertainties.

In Chapter 3 we develop of a Bayesian hierarchical model for joint nonstationary precipitation and streamflow frequency analysis in rainfall-runoff dominated basins such as those in the southwest US. Peak streamflow is modeled as a consequence of spatial precipitation extremes, allowing for temporal nonstationarity from climate covariates.

In Chapter 4 we develop a general hierarchical Bayesian multivariate nonstationary frequency analysis framework with an application to dam safety analysis. In this, the peak snow depth and peak streamflow are linked to reservoir water level and, consequently, dam safety.

Conclusions and future work are provided in Chapter 5.

Chapter 1

Spatial Variability of Seasonal Extreme Precipitation in the Western United States

Abstract

We examine the characteristics of 3-day total extreme precipitation in the Western United States. Coherent seasonal spatial patterns of timing and magnitude are evident in the data, motivating a seasonally based analysis. Using a clustering method that is consistent with extreme value theory (EVT), we identify coherent regions for extremes that vary seasonally. Based on storm back trajectory analysis, we demonstrate unique moisture sources and dominant moisture pathways for each spatial region. In the winter the Pacific ocean is the dominant moisture source across the west, but in other seasons the Gulf of Mexico, the Gulf of California, and the land surface over the Midwestern US play an important role. We find the El Niño Southern Oscillation (ENSO) to not have a strong impact on dominant moisture delivery pathways or moisture sources. The frequency of extremes under ENSO is spatially coherent and seasonally dependent with certain regions tending to have more (less) frequent extreme events in El Niño (La Niña) conditions.

1.1   Introduction

The nature of extreme precipitation varies widely across the Western United States. For example, the Southwest is most likely to receive extreme precipitation in the summer, while the Pacific Northwest and California typically see the largest extreme events in the winter, and the intermountain west tends to see a more even distribution of occurrence across seasons [*Kunkel et al.*, 1999]. The mean occurrence day of annual maxima for all stations in the Western US clearly shows a peak in the winter months (DJF), but in more than 50% of stations, annual maxima tend to occur between February and July (Figure 1.1). This motivates a careful examination of how extremes behave both seasonally and spatially. Past studies have classified the behavior of extreme events regionally throughout the Western US [*Groisman et al.*, 2001; *Arriaga Ramírez and Cavazos*, 2010; *Dos Santos et al.*, 2011; *Dulière et al.*, 2013a; *Mullens et al.*, 2013; *Janssen et al.*, 2014] and for specific seasons [*Warner et al.*, 2012; *Pal et al.*, 2013; *Jiang et al.*, 2014], but few have taken a detailed look at both of these pieces. A seasonal analysis is especially important because while the most likely season for an extreme event may be identified for a specific region, extreme events can occur at any time of the year and the characteristics of these events vary both seasonally and spatially [*Kunkel et al.*, 1999].

Extreme precipitation takes many forms in the Western US due to complex topography and climatic interactions. Figure 1.2 shows the average magnitude within each season and the average occurrence day from the beginning of the season of 3-day extreme events for all stations in the Western US (see Section 2 for a complete description of the data). A high degree of variability is present spatially and between seasons in both the average timing and magnitude of extreme events in the Western US and motivates further investigation. In terms of statistical distributions of extreme events, two weather stations close enough to identically observe all the same events would necessarily have the same extreme value distributions. Two stations further apart might observe some of the same extreme events but the events might differ in magnitude, perhaps causing the extreme value distributions to have the similar shape but have slightly different means.
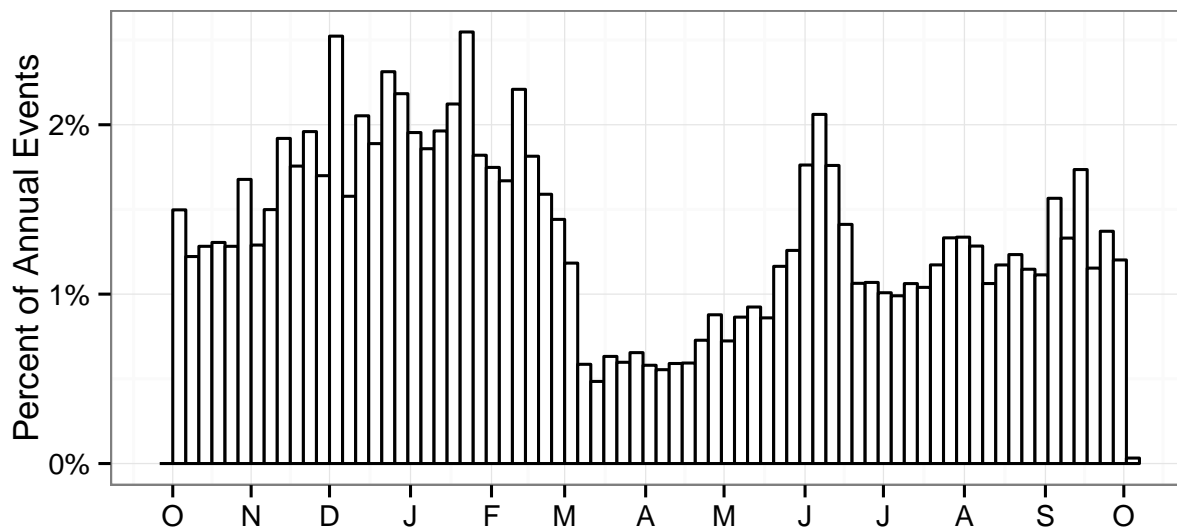
Figure 1.1: Occurrence day of annual 3-day precipitation maxima at ∼14,000 stations in the western US (5 day bins).

Two stations very far apart, not observing any of the same events and having different climatologies, would exhibit different statistical distributions, except by chance. How far need we go such that the extreme value distributions at two weather stations no longer resemble each other and is it possible to create groups of weather stations, or regions, such that the distributions looks sufficiently similar? This grouping, or clustering, is a straightforward way of identifying regions for which extreme values behave similarly [*Hsu and Li*, 2010].

Past studies have grouped stations by climate divisions [*Kunkel*, 2003b], though these regions are defined for climatological mean and are not appropriate for extreme values [*Jones et al.*, 2014]. Other studies have used grid based groupings [*Kunkel et al.*, 2003], subjective [*Maraun et al.*, 2008; *Alexander et al.*, 2006] and objective [*Jones et al.*, 2014; *Wigley et al.*, 1984; *Dales and Reed*, 1989; *Neal and Phillips*, 2009] regions. *Jones et al.* [2014] defined regions in the UK using principal component analysis and clustering of a number of extreme value statistics. *DeGaetano* [1998] used a method for defining clusters based on similarity of extreme value cumulative distributions function and spatial proximity. *Bernard et al.* [2013] used a clustering method specifically tailored to

the characteristics of extreme value distributions.

Given homogeneous clusters of extreme precipitation, dominant moisture pathways and sources of extreme precipitation can be examined regionally. Moisture pathway and delivery questions can be answered with back trajectory analysis. Back trajectory analysis calculates the pathway that an air parcel followed such that it arrives at the location and time of an observed extreme event. Trajectory analysis has been used previously to identify moisture sources and pathways for extreme precipitation [*Gustafsson et al.*, 2010; *Massacand et al.*, 1998; *Reale et al.*, 2001; *Alexander et al.*, 2015]. In this study we investigate the statistically likely moisture sources and pathways for extreme events and how these vary between seasons and between regions [*De-Gaetano*, 1998; *Jorba et al.*, 2004]. This is of importance in modeling, simulating, and predicting extremes in space and time and, consequently, for resource management.

In addition to a seasonal analysis, we also seek to understand the impact of the El Niño Southern Oscillation (ENSO) on dominant moisture pathways and sources in the Western US. The link between ENSO and extreme events has been previously explored [*Gershunov and Barnett*, 1998; *Cayan et al.*, 1999; *Higgins et al.*, 2010; *Feldl and Roe*, 2011; *DeFlorio et al.*, 2013]. In El Niño conditions, days with high daily precipitation are seen to be more frequent than average over the Southwest and less frequent over the Northwest. During La Niña conditions the signal is typically reversed, but the ENSO events are not all the same and the spatial patterns are complex.

We propose the following research questions related to extreme events in the western US:

- Can we objectively define coherent extreme value regions and how many regions are appropriate?

- What are the dominant moisture sources and pathways for each season for these regions?

- How do seasonal moisture sources pathways change under ENSO regimes?

This paper is structured as follows: We discuss data sources and preprocessing in section 2, methods in section 3, results in section 4, and discussion and conclusions in section 5.
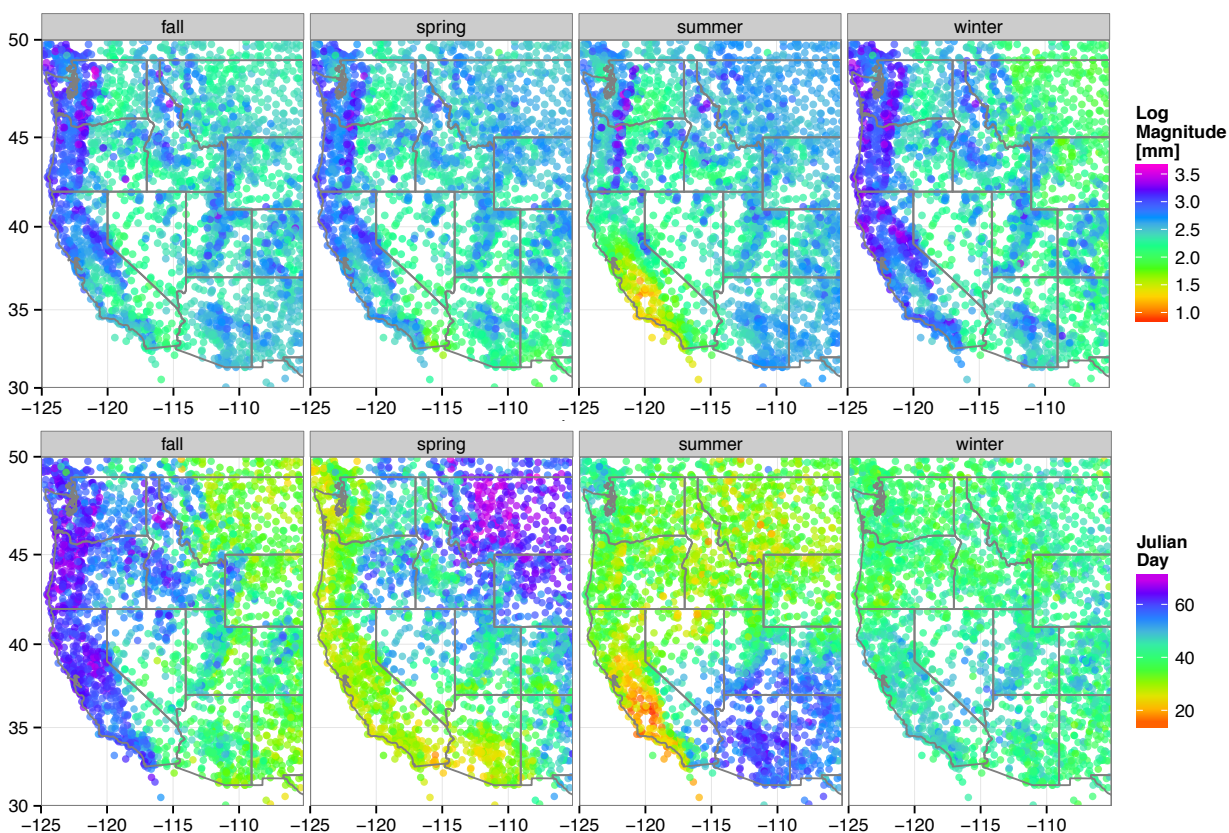
Figure 1.2: Mean magnitude (top) and Timing (bottom) of extreme events in the western US. In the top graphic, Color indicates magnitude on a log scale. In the bottom graphic, color indicates the average Julian day of occurrence of maxima at a station from the start of the season. For corresponding standard deviation point maps, please see the supplemental material.

1.2   Data and Preprocessing

1.2.1   Precipitation Data

We obtained daily precipitation data from the Global Historical Climatology Network (GHCN, http://www.ncdc.noaa.gov/oa/climate/ghcn-daily/) [*Durre et al.*, 2008, 2010; *Menne et al.*, 2012]. Of the approximately 13,000 stations falling in the study region, we included only those stations with greater than 75% data coverage (at least 50 years of data) from 1948-2013, leaving us with 1,037 stations.

An extreme precipitation dataset was developed using a seasonal block maxima approach.

Seasons were defined as three month blocks: winter (DJF), spring (MAM), summer (JJA), and fall (SON). For each station, Seasonal 3-day maxima were computed for each year in the record. The extreme events were compiled into a database of approximately 600,000 events.

1.2.2   Back trajectories

For each event, back trajectories were computed using the HYSPLIT trajectory model [*Draxler et al.*, 1999; *Draxler and Hess*, 1998, 1997]. A back trajectory is a three dimensional pathway taken by a parcel of air such that it arrives at a particular location at the time of a known extreme event. Back trajectories are commonly used in air pollution modeling, but they have also been used for moisture source identification [*Lu et al.*, 2013; *Izquierdo et al.*, 2012; *Gustafsson et al.*, 2010; *Jorba et al.*, 2004; *Stohl and Trickl*, 1999]. HYSPLIT requires gridded climate data to calculate back trajectories, as well as a terminal time and location for the back trajectory. We use the NCEP/NCAR reanalysis data [*Kalnay et al.*, 2011].

The upper limit on residence time of moisture in the atmosphere is approximately 8 days [*Trenberth*, 1998]. In addition, for trajectories computed from wind fields, errors of 20% the distance traveled are expected [*Stohl and Seibert*, 1998; *Stohl*, 1998]. Given this uncertainty and the limit on moisture retention, trajectory locations were computed hourly for 8 days preceding the extreme event (192 hours). Trajectories were initialized for each event every 6 hours during the event period and at 500m vertical intervals from 0m to 5,000m above ground level (totaling 151 trajectories per event). The results were compiled into a database of approximately 8,000,000 trajectories.

1.3   Methods

1.3.1   Identification of Extremes Regions

Clustering is an intuitive method for grouping multivariate data. In classical *k*-means clustering, clusters are determined so that they minimize the intracluster variance of a metric related

to Euclidian distance. For example, if points in the plane are clustered based only on x and y position, the k-means algorithm creates k clusters that minimize the variance of the distance between each point in a cluster. Cluster centers are determined by taking the mean of all cluster member points, and thus the center of each cluster may not be located at a point in the cluster. The k-means method excels at identifying patterns related to mean behavior of Gaussian or Gaussian mixture data, but in the context of extreme values, k-means clustering is inappropriate for two reasons [*Bernard et al.*, 2013].

(1) With k-means, clusters are developed based on the mean of observations within a cluster. With Gaussian data this poses no problem since the mean of Gaussian data remains Gaussian. When applying k-means to highly skewed extreme value data, k-means centroids are not interpretable, since the mean of Generalized Extreme Value (GEV) data is Gaussian and not GEV. The solution to this issue is to use an alternative clustering algorithm called partitioning around medoids (PAM) [*Kaufman and Rousseeuw*, 1990]. This method creates clusters that are centered around an existing station and requires no averaging, and therefore alleviates the interpretation issue.

(2) The classical methods of assessing pairwise dependence between time series (i.e. Euclidian distance) are not in compliance with extreme value theory (EVT) when applied to time series of maxima [*Bernard et al.*, 2013]. The solution to this issue is the use a measure of pairwise dependence called the F-Madogram, which is explicitly tailored to extremal data. This measure of dependence can be used as the distance matrix in the PAM clustering algorithm, creating an theoretically sound extreme value clustering method.

Further explanation of item 2 above is necessary. Using a variogram called the F-Madogram, it is possible to construct a measure of pairwise dependence that is appropriate for extreme values [*Naveau et al.*, 2009; *Cooley et al.*, 2006]. Given T samples of bivariate maxima $(M_i^{(t)}, M_j^{(t)})^T$ from two locations i and j, the nonparametric estimator for the F-madogram is given by *Bernard et al.*

[2013] as

$$\hat{d}_{ij} = \frac{1}{2T} \sum_{t=1}^{T} \left| \hat{F}_i(M_i^{(t)}) - \hat{F}_j(M_j^{(t)}) \right|, \tag{1.1}$$

where

$$\hat{F}_i(u) = \frac{1}{T} \sum_{t=1}^{T} \mathbf{1}_{\{M_i^{(t)} \leq u\}} \tag{1.2}$$

where $\mathbf{1}_{\{M_i^{(t)} \leq u\}}$ is the indicator function for the event $\{M_i^{(t)} \leq u\}$ which returns 1 if the statement is true or 0 otherwise. The entire function returns a proportion of the number of data points that are less than or equal to a given value u (the empirical cumulative distribution function (CDF)). It is important to note that the F-madogram does not depend on the magnitude of extreme events, providing a dimensionless metric that compares the shape of the extreme value distributions between two stations. Coupled with the PAM algorithm, the F-madogram provides an efficient, nonparametric, and theoretically sound method for clustering maxima.

Bernard et al. [2013] applied this extreme value oriented clustering method to station data covering France with favorable results. Since this method is based on only the shape of the extreme value distribution at a station and not on magnitude of event or geographic proximity, as physical extent of a region increases, so does the chance of misclassification of a station. In other words, extreme value distributions from two geographically disparate stations may look the same for different physical reasons. To address this issue we propose an extension to the clustering algorithm that also incorporates physical proximity of stations. The extension involves computing a modified version of the madogram

$$\hat{\hat{d}}_{ij} = \hat{d}_{ij} + p_{ij}, \tag{1.3}$$

where

$$p_{ij} = \frac{q_{ij}}{\sum_{i=1}^{N} q_{ij}} \max_{ij} \hat{d}_{ij} \tag{1.4}$$

and

$$q_{ij} = \sqrt{(x_i - x_j)^2 + (y_i - y_j)^2}. \tag{1.5}$$

The computation of p_{ij} is simply the Euclidian distance between the station locations scaled such that they will never exceed the largest value of the original *F*-madogram. Note that the Euclidian distance formula may be replaced with the Haversine distance formula if the original data is not projected.

We present a comparison of the original clustering algorithm of *Bernard et al.* [2013] (Figure 1.3, top) and the same algorithm with our improvements (Figure 1.3, bottom). Both graphics use only stations with near-complete record from 1950-2014 and 8 clusters are specified. In the original algorithm, few clusters are physically contiguous. We still see similar clustering regions defined in both algorithms, but the inclusion of a weighted distance matrix into the clustering algorithm greatly improved the cluster coherence.

As a final step in determining extreme regions, we extended the clusters based on point data to cover the entire study region, so that any stations that did not have sufficient data to be included in the clustering can be associated with a cluster. This was achieved by using a Dirichlet tessellation (or Voronoi tessellation) of the points included in the clustering algorithm, attributing all the area closest to a station as part of that station's cluster. Note that a region need not be contiguous, though they typically are.

1.3.1.1 Choosing the number of clusters

For the PAM clustering method, the metric typically used for choosing a relevant number of clusters is called the silhouette coefficient [*Rousseeuw*, 1987]. Though several metrics exist for aiding in the determination of the number of clusters required in a nonhierarchical clustering algorithm, the choice always comes down to an application-based subjective decision [*DeGaetano*, 2001]. For our application we wanted to choose the number to be the same for all seasons for the
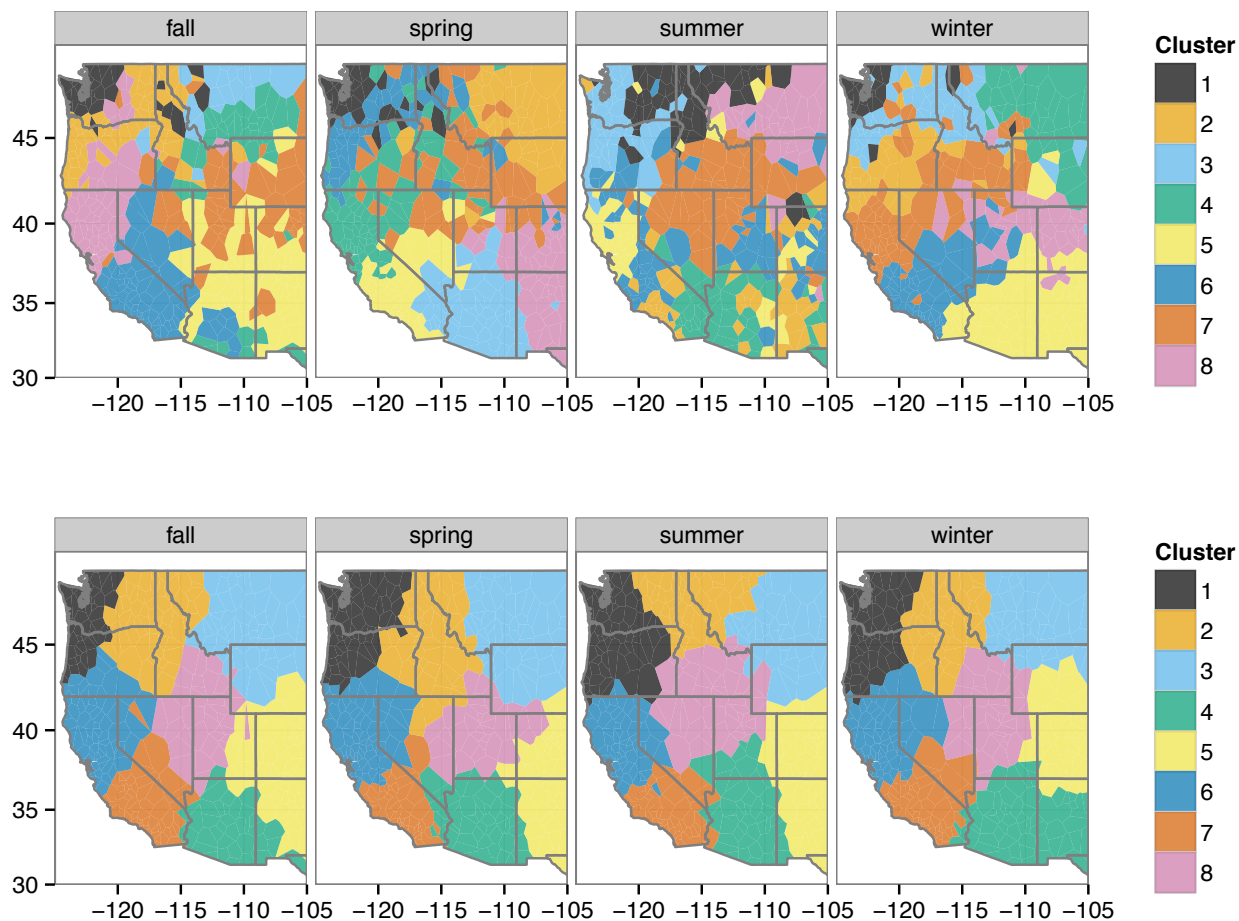
Figure 1.3: (top) Extreme regions defined by the clustering method of *Bernard et al.* [2013] and (bottom) regions defined with the modified extremes clustering method for large geographic regions.

purposes of comparing across seasons, near-optimal in terms of the silhouette coefficient, reasonably resolute, and manageable from a data analysis perspective. The choice of 8 clusters satisfied these criteria, yet any number of clusters from 6–11 would have been reasonable. Clusters defined with this method exhibit self similarity in that the same clustering method could be applied again to a single region, further defining more resolute regions.

1.3.2   Moisture Source Identification

To identify moisture sources we started by filtering trajectories by those that produced precipitation. We included 100 trajectories per station from each season that (1) produced the greatest

decrease in specific humidity along a trajectory during the event period and (2) dropped below 1000m at some point during the 8 day window. We required a height threshold so that we excluded trajectories that did not pick up moisture during the 8 day window. The loss of specific humidity coupled with the observed maxima provides a high degree of confidence that the selected subset of trajectories produced precipitation at the surface. We refer to this subset as the 'rain trajectories.'

The source region identification method is somewhat imprecise, technically providing the end of the source region. *Gustafsson et al.* [2010] identified the beginning of a source region as the first time the specific humidity of a trajectory drops below its ending specific humidity. We found this criteria difficult to apply since in many cases our ending specific humidity was close to zero. Given the inaccuracy of a single trajectory, using the point where maximum specific humidity occurred was a sufficiently good indicator of source region location.

From the set of rain trajectories, we identified a moisture source location by the point at which a trajectory achieved its maximum specific humidity. Minimum physical height would have also been a reasonable indicator; initial exploration indicated that these two indicators gave nearly identical results. Computing moisture source locations for each rain trajectory and binning the resulting locations on a 1 degree grid, we get a picture of moisture source regions for a given cluster and season.

1.3.3 Trajectory Clustering

Trajectory clustering is a well known statistical method for analyzing moisture transport patterns from trajectory data [*Moody and Galloway*, 1988; *Moody*, 1986; *Stohl*, 1998; *Dorling et al.*, 1992]. The method is an application of the *k*-means clustering algorithm to longitudinal data [*Genolini and Falissard*, 2010] and is implemented in the KmL package [*Genolini and Falissard*, 2011]. We used the Haversine distance formula for calculating intra-cluster root mean squared error (RMSE).

We fixed the number of clusters in each region and season to 10 – the aim was to explore

groups produced with a fixed number of clusters. For each group we determined an average trajectory as the mean of all the trajectory locations at a given time.

To investigate the ENSO connection we identified events based on the multivariate ENSO index (MEI) [*Wolter and Timlin*, 1998, 1993] (http://www.esrl.noaa.gov/psd/enso/mei/). A season was identified as having strong El Niño or La Niña conditions if the MEI value was greater than 1 or less than -1, respectively. Trajectories were composited based on this ENSO classification to identify the teleconnections.

1.4   Results

1.4.1   Cluster Descriptions

Clusters were similar between seasons but not identical - the boundaries shift seasonally indicating differences in extreme distributions across seasons. Remarkably, the centroids of each region fell near the same location for each cluster (Figure 1.3 bottom). This is coincidental since each season is clustered independently, but we leveraged this to describe the regions across seasons. Each region is prefixed with a label that will be used to refer to the region.

1. (PNW) Western Oregon and Washington roughly extending east to the Cascade Range

2. (PNE) Eastern Oregon and Washington and Western and Northern Idaho and far Western Montana

3. (MT) Eastern Montana and Northern Wyoming

4. (AZ) Arizona and in winter, New Mexico

5. (CB) Western Colorado, Eastern Utah, Southern/Central Wyoming and New Mexico (in fall, spring and summer only)

6. (NC) Northern California, Southern Oregon and Western Nevada

7. (SC) Southern California and Southern Nevada

8. (GB) Great Basin watershed including Western Utah, Eastern Nevada and Southern Idaho

1.4.2 Moisture Sources

Figure 1.4 shows moisture source regions for each cluster and season. In winter, not surprisingly, more than 98% of moisture sources for extremes are in the Central to Eastern Pacific Ocean (including the Gulf of California). In coastal clusters (PNW, NC, SC) moisture tends to be picked up further from the coast than inland clusters (PNE, MT, AZ, CB, GB).

In summer a few patterns stand out. Moisture is generated in a band of the Northwest Pacific that can extend to the far Western Pacific (PNW, PNE, MT, NC, SC, GB). This pattern can be seen in all clusters except for the southwest clusters (AZ, CB). In southwest clusters (AZ, CB), the near-coast Eastern Pacific, the Gulf of California, and the Gulf of Mexico appear as dominant moisture sources. A somewhat surprising result is the dominance of the land as a moisture source for inland clusters (PNE, MT), likely due to a combination of moisture transport and moisture recycling [*Bosilovich and Schubert*, 2001; *Dirmeyer et al.*, 2014]. The inland cluster GB exhibits a mixture of all the summer patterns.

Spring and fall can be viewed as transitionary seasons between summer and winter. All of the previously described patterns are present in varying degrees. In coastal clusters (PNW, NC), due to the direct influence of the Pacific Ocean, we found the transition between summer and winter to be much less strong than in inland clusters (MT, for example).

1.4.3 Moisture Pathways

Figure 1.5 shows the dominant pathways for extremes in the Western US and Table 1.1 shows the percentage of trajectories included in each trajectory group. Winter pathways typically run from the winter moisture sources, i.e. the Central to Eastern Pacific, directly onto land for all clusters. Many winter pathways for coastal regions (PNW, NC, SC) follow well known atmospheric river (AR) patterns [*Newell et al.*, 1992; *Zhu and Newell*, 1998; *Ralph and Dettinger*, 2011; *Neiman et al.*, 2011; *Villarini et al.*, 2013; *Alexander et al.*, 2015]. With few exceptions, pathways for
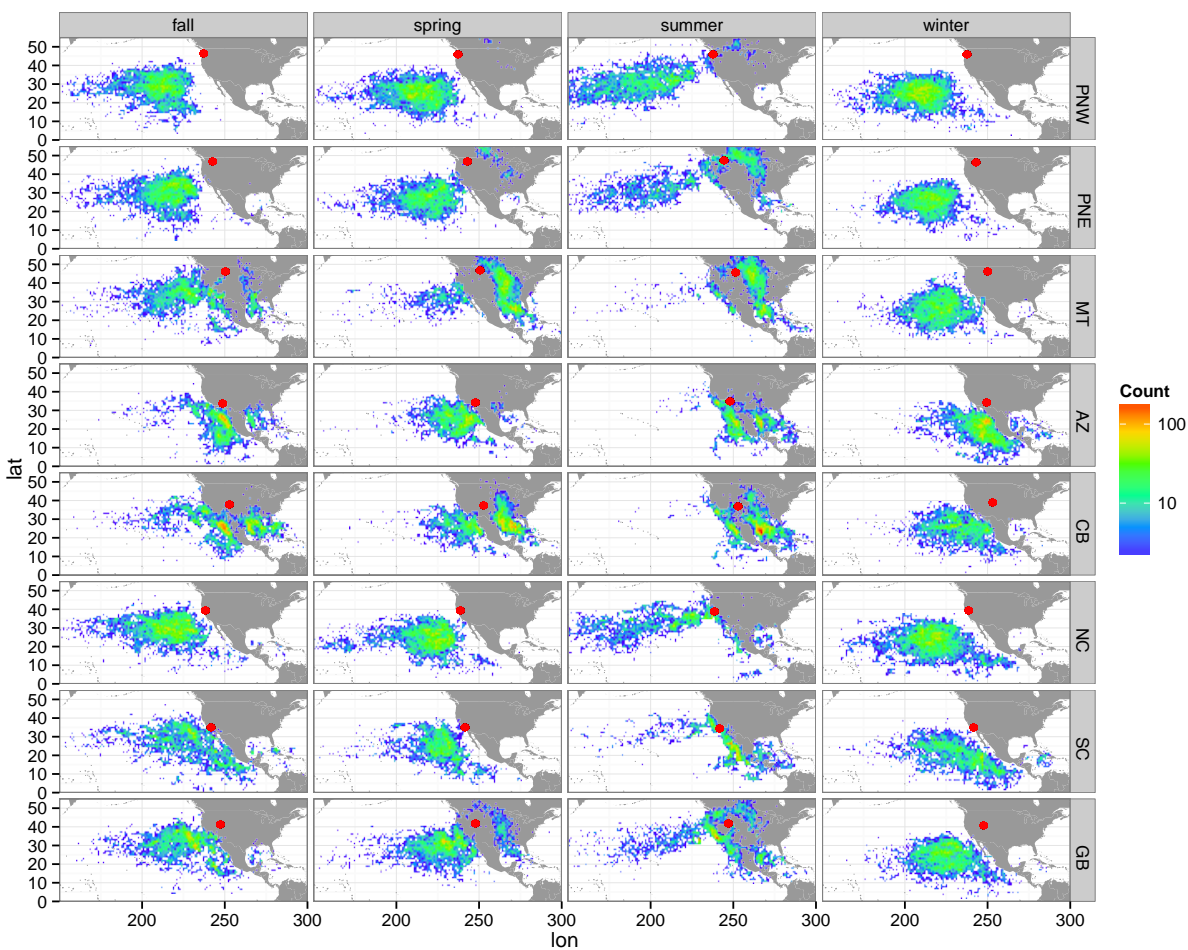
Figure 1.4: Moisture source location counts for each season and region, binned on a 1° grid. Red dots indicate the center of each extreme region.

the coastal regions (PNW, NC, SC) mimic winter, while the more inland regions (PNE, MT, AZ, CB, GB) display pathways from the Gulf of Mexico, north over land and from the Gulf of California. Summer pathways display the most diversity; for example, regions MT and CB display numerous distinct pathways. Fall and spring pathways appear as a transition from summer to

Table 1.1: Percentage of trajectories included in each group by region and season.

Season	Region	Trajectory Group									
		A	B	C	D	E	F	G	H	I	J
fall	PNW	20.53	16.26	14.15	9.70	9.59	9.25	7.67	7.39	5.29	0.18
fall	PNE	15.95	15.25	14.27	13.41	10.36	7.87	5.93	5.69	5.63	5.62
fall	MT	19.17	16.34	12.93	10.30	10.19	9.19	7.05	5.84	4.89	4.10
fall	AZ	21.23	18.33	15.77	13.96	9.31	7.24	6.70	5.44	1.85	0.16
fall	CB	23.43	18.25	15.57	12.43	12.23	7.62	4.45	4.24	1.77	0.01
fall	NC	22.21	12.45	12.42	10.57	10.38	8.43	7.56	7.37	5.19	3.41
fall	SC	28.72	15.63	11.68	11.01	10.95	7.89	5.85	5.06	3.19	0.00
fall	GB	21.81	15.55	15.03	10.09	9.07	8.06	7.67	5.29	4.31	3.12
spring	PNW	16.75	16.74	11.99	11.72	10.75	9.86	9.59	5.71	4.86	2.02
spring	PNE	18.07	17.08	14.87	10.43	8.60	8.50	8.26	5.35	5.11	3.73
spring	MT	16.55	14.99	13.91	10.42	10.24	9.56	9.28	9.01	4.10	1.94
spring	AZ	27.27	21.96	17.72	9.55	6.08	4.82	4.64	3.41	2.91	1.63
spring	CB	20.31	15.58	13.51	12.89	10.16	9.64	6.32	5.06	3.77	2.75
spring	NC	20.75	18.83	12.50	11.14	11.02	10.93	6.99	5.06	2.77	0.00
spring	SC	20.27	15.97	14.14	9.97	9.20	8.16	7.99	7.72	4.46	2.12
spring	GB	23.07	16.63	13.23	10.77	8.95	7.76	7.66	5.35	3.56	3.02
summer	PNW	26.50	16.25	15.53	10.21	8.94	8.68	7.74	2.65	2.44	1.05
summer	PNE	25.28	17.05	14.03	9.53	8.64	7.40	6.34	6.12	3.30	2.32
summer	MT	25.31	18.82	16.11	13.57	8.92	5.64	4.72	4.52	1.53	0.88
summer	AZ	19.23	17.33	15.12	14.87	12.77	9.18	5.95	3.42	1.75	0.39
summer	CB	23.14	14.54	14.24	12.29	10.77	9.65	7.36	6.07	1.91	0.00
summer	NC	15.47	15.38	13.01	12.09	9.55	9.45	8.50	6.86	5.18	4.50
summer	SC	21.38	20.65	14.62	11.04	9.30	6.76	5.48	4.09	3.58	3.11
summer	GB	22.12	19.38	15.53	10.38	10.04	9.98	6.98	5.34	0.00	0.00
winter	PNW	21.90	13.95	12.86	11.65	11.39	11.27	8.07	6.54	2.17	0.19
winter	PNE	21.53	18.51	12.54	11.81	9.06	8.52	8.01	4.67	3.62	1.72
winter	MT	20.12	16.71	13.66	11.94	9.33	8.69	5.78	4.85	4.81	4.10
winter	AZ	21.96	17.69	16.06	15.49	11.20	8.98	2.95	2.87	2.79	0.01
winter	CB	23.33	15.76	15.45	13.84	12.95	6.68	6.50	2.48	2.43	0.58
winter	NC	18.81	16.69	16.48	14.49	9.34	8.74	6.63	4.51	3.11	1.20
winter	SC	17.86	17.24	16.08	15.36	10.92	7.38	6.40	4.61	2.89	1.25
winter	GB	25.45	20.81	18.04	11.40	7.61	6.29	4.30	3.81	1.96	0.33

winter, as with the moisture sources.

1.4.4   ENSO Connections to Extremes

From a back trajectory perspective, we examined the effects of ENSO on the frequency of extremes. Figure 1.6 shows the ratio of trajectories occurring in La Niña versus El Niño years.
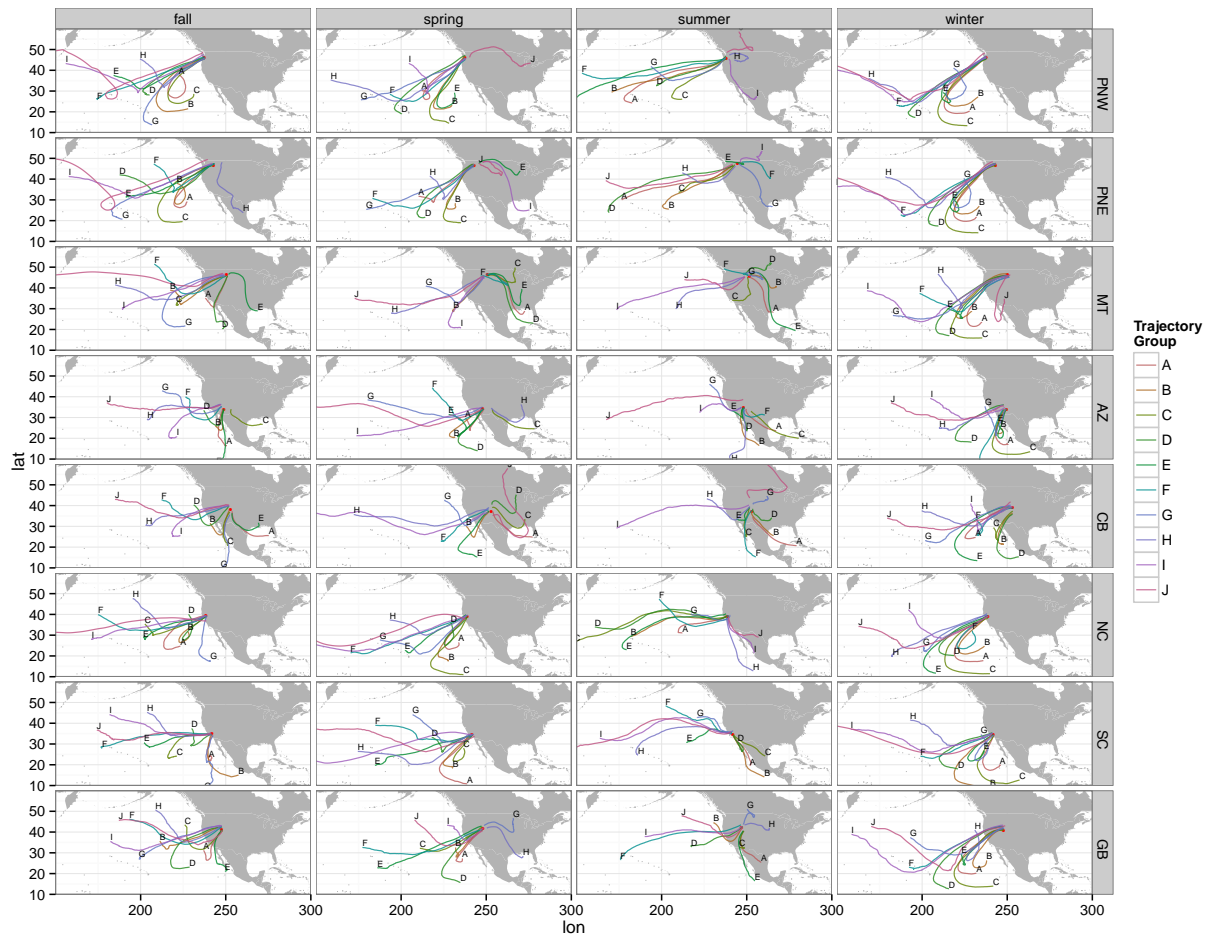
Figure 1.5: Dominant pathways (determined by trajectory clustering) by region and season.

A value greater than 1 (blue) indicates that a station is Niña dominated (experiences relatively more strong events in La Niña conditions) and a value less than 1 (red) indicates that a station is Niño dominated (experiences more events in El Niño conditions). A north/south divide can be seen in both summer and winter, the north being predominately Niña dominated and the south being predominantly Niño dominated. The signal is more mixed in the fall and spring. Southern California is always Niño dominated and Western Oregon is always Niña dominated. Similar north-south dipoles have been documented in [*Cayan et al.*, 1999] and [*Feldl and Roe*, 2011] although a direct comparison was not possible because of dissimilar time windows.
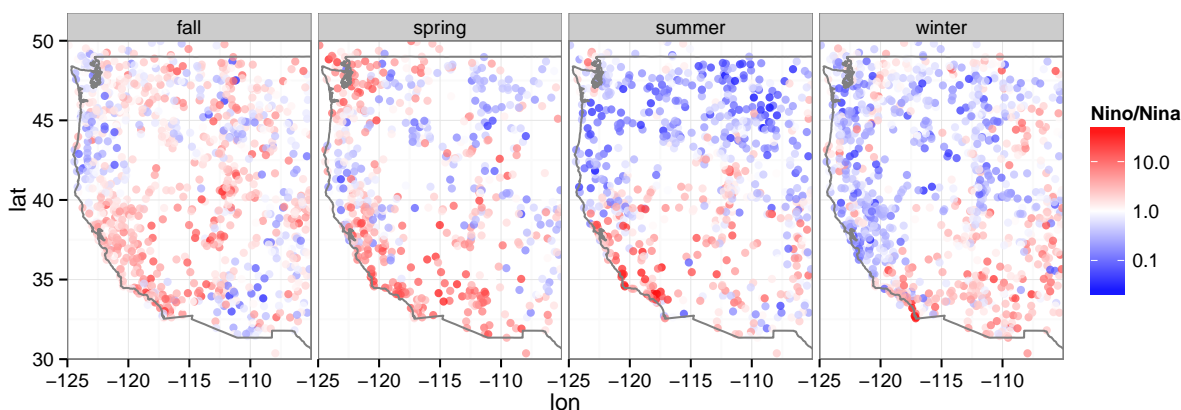
Figure 1.6: Ratio of the number of rain trajectories occurring in La Niña versus El Niño years. For points in red, more rain trajectories occurred in El Niño seasons and for points in blue, more rain trajectories occurred in La Niña seasons.

We did not find ENSO to have a strong effect on moisture source locations. We found ENSO to affect trajectory pathways but typically only prior to a moisture source location, indicative of ENSO's influence on larger atmospheric circulation patterns. Moisture source locations and delivery pathways from moisture sources to event locations remained essentially unchanged. See the supplementary material for additional graphics.

1.5   Discussion and Conclusions

We have presented a detailed analysis of 3-day total extreme precipitation throughout the western United States. Using an improved extreme value clustering method, we defined spatially coherent regions for extremes that vary seasonally and made physical sense based on topography. Based on storm back trajectory analysis, we were able to demonstrate unique moisture sources and dominant moisture pathways for each spatial region.

Winter and summer extremes display distinct patterns of moisture delivery, timing, and magnitude throughout the western US. In these terms, winter extremes behave mostly uniform

across the west, while summer extremes display a much higher degree of spatial variability. Fall and spring manifest as transition periods between these two regimes. In addition to the Pacific Ocean (including the Gulf of California), The Gulf of Mexico appears as a moisture source predominantly for inland clusters in fall, spring and summer. For northeastern regions mostly covering Wyoming and Montana, the land surface is a dominant moisture source. Coastal regions including Northern California, Oregon, and Washington source nearly all moisture directly from the Pacific Ocean. In the summer, southwest regions including Southern California, Arizona, New Mexico, and Western Colorado tend to have multiple dominant moisture pathways from both the Gulf of Mexico, Gulf of California, and the Pacific Ocean.

ENSO had little effect on moisture sources; moisture pathways were typically only affected prior to moisture source locations. The occurrence frequency of extremes under ENSO conditions is spatially coherent and seasonally dependent with certain regions tending to have more or less extreme events depending on El Niño or La Niña conditions.

To more precisely determine moisture source locations, the method for determining source region locations could be improved, although using higher resolution reanalysis data would likely be a better fist step. We were not able to determine the proportion of moisture that is gained from land versus open water, an apportionment which could be useful in more detailed studies. In addition, when multiple moisture sources are present for a single region, a more detailed analysis would be required to determine the degree to which certain moisture sources are active in ENSO conditions.

By only including trajectories with moisture sources during the 8 day back trajectory, we excluded trajectories that started the 8 day period with high specific humidity. There are likely extreme events produced by air that gains moisture prior to the 8 day window, but we did not have the means to identify those sources.

The NCEP reanalysis has a very coarse (2.5 degree) resolution and thus details of the pathways, such as the specific paths through the mountains, are not well resolved. For this study, the level of detail was sufficient, but we could identify higher resolution features such as specific

pathway through mountains [*Alexander et al.*, 2015]. The use of newer (and shorter duration) re-analysis such as the ERA-interim [*Dee et al.*, 2011], the Climate Forecast System Reanalysis (CFSR) [*Saha et al.*, 2010], the Modern-era Retrospective Analysis for Research (MERRA) [*Bosilovich et al.*, 2012], or the North American Regional Reanalysis (NARR) [*Mesinger et al.*, 2006] would allow us to examine pathways in more detail.

This analysis opens the door to many new applications. By sampling the trajectory data conditioned on features such as current location of trajectories, sea surface temperatures, etc., short term projections of spatially coherent extremes can be made. This resampling is akin to generating hurricane tracks [*Yonekura and Hall*, 2011, for example]. The trajectory projections can be coupled with spatial extremes model [*Cooley et al.*, 2007, for example] to produce return level maps of extreme precipitation, and consequently hydrologic extremes, important for resource management. Furthermore, these trajectories can be resampled to produce physically based simulations of extreme precipitation. We can also investigate the climatic conditions in moisture source regions that favor the production of extremes, potentially to develop statistical forecast models. Finally, given the evidence of the land surface as a moisture source for some regions, we would like to investigate the relative contribution of the land surface versus open water bodies as a moisture source for extreme precipitation.

oa/climate/ghcn-daily/). The NCEP/NCAR reanalysis used in this study is available in HYS-PLIT format from the NOAA ARL ftp server (`ftp://arlftp.arlhq.noaa.gov/pub/archives/reanalysis`).

Observed data and computed trajectories are available at: `http://bechtel.colorado.edu/~bracken/western-us-extremes-data/` .

Chapter 2

Spatial Bayesian hierarchical modeling of precipitation extremes over a large domain

Abstract

We propose a Bayesian hierarchical model for spatial extremes on a large domain. In the data layer a Gaussian elliptical copula having generalized extreme value (GEV) marginals is applied. Spatial dependence in the GEV parameters are captured with a latent spatial regression with spatially varying coefficients. Using a composite likelihood approach, we are able to efficiently incorporate a large precipitation dataset, which includes stations with missing data. The model is demonstrated by application to fall precipitation extremes at approximately 2600 stations covering the western United States, -125E to -100E longitude and 30N to 50N latitude. The hierarchical model provides GEV parameters on a 1/8th degree grid and consequently maps of return levels and associated uncertainty. The model results indicate that return levels vary coherently both spatially and across seasons, providing information about the space-time variations of risk of extreme precipitation in the western US, helpful for infrastructure planning.

2.1 Introduction

Engineering design of infrastructure such as flood protection, dams, and management of water supply and flood control require robust estimates of return levels and associated errors of precipitation extremes. Spatial modeling of precipitation extremes not only can capture spatial dependence between stations but also reduce the overall uncertainty in at-site return level estimates by borrowing strength across spatial locations [*Cooley et al.*, 2007]. Hierarchical Bayesian

modeling of extremes precipitation was first introduced by [*Cooley et al.*, 2007] and since has been widely discussed in the literature [*Cooley and Sain*, 2010; *Aryal et al.*, 2010; *Atyeo and Walshaw*, 2012; *Davison et al.*, 2012; *Ghosh and Mallick*, 2011; *Reich and Shaby*, 2012; *Sang and Gelfand*, 2010, 2009a; *Apputhurai and Stephenson*, 2013; *Dyrrdal et al.*, 2014]. Hierarchical modeling is an alternative to regional frequency analysis providing gridded or pointwise estimates of return levels within a study region [*Renard*, 2011].

Bayesian hierarchical models for spatial extremes have typically been limited to small geographic regions that include on the order 100 stations covering areas on the order of 100,000 km^2. Large geographic regions with many stations present a computational challenge for hierarchical Bayesian models, specifically when computing the likelihood of Gaussian processes (GPs), which for n data points requires solving a linear system of n equations, an $O(n^3)$ operation. Several approaches exist for speeding up GP likelihood computations such as low-rank approximations [*Banerjee et al.*, 2008], composite likelihood methods [*Lindsay*, 1988; *Heagerty and Lele*, 1998; *Caragea and Smith*, 2007; *Varin et al.*, 2011], spectral methods [*Fuentes*, 2007], restricted likelihoods [*Stein et al.*, 2004] and Laplace approximations [*Rue et al.*, 2009]. The use of a composite likelihood approach is explored here because we not only wish to estimate covariance parameters but to also produce maps of return levels with small credible intervals.

Some attempts have been made to model extremes in large regions and with large datasets in a Bayesian hierarchical context. *Reich and Shaby* [2012] use a hierarchical max-stable model with climate model output in the east coast to examine spatially varying GEV parameters, with a max-stable process for the data dependence level. [*Ghosh and Mallick*, 2011] model gridded precipitation data over the entire US, for annual maxima at a 5x5 degree resolution (43 grid cells) and copula for data dependence, incorporating spatial dependence directly in a spatial model on the data, not parameters. [*Cooley and Sain*, 2010] and [*Sang and Gelfand*, 2009a] model over 1000 grid cells of climate model output using spatial autoregressive models which take advantage of data on a regular lattice to simplify computations.

The research contributions of this study are as follows. A Bayesian hierarchical model is

proposed which is capable of incorporating thousands of observation locations by utilizing a composite likelihood method. The GEV shape parameter is modeled spatially in order to capture the detailed behavior of extremes in the western US. In addition the model is capable of incorporating stations with missing data with little additional computational overhead. The model is applied to observed precipitation extremes in each season, providing estimated seasonal return levels for the western US.

In section 2 the general model structure is described. Section 3 describes details of the application to seasonal extreme precipitation in the western US. Results are discussed in Section 4 and Discussion and conclusions are given in Section 5.

2.2   Model structure

The joint distribution of the m stations in each year is modeled as a realization from a Gaussian elliptical copula with generalized extreme value (GEV) distribution marginals. The copula is characterized by pairwise dependence matrix Σ. Spatial dependence is further captured through spatial processes on the location $\mu(\mathbf{s})$, scale $\sigma(\mathbf{s})$ and $\xi(\mathbf{s})$ parameters. We assume the parameters can be described through a latent spatial regression where the residual component $w_\gamma(\mathbf{s})$ follows a mean 0, stationary, isotropic Gaussian process (GP) with covariance function $C_\gamma(\mathbf{s}, \mathbf{s}')$ where γ represents any GEV parameter (μ, σ, ξ). The corresponding covariance matrix is $C_\gamma(\boldsymbol{\theta}_\gamma) = [C_\gamma(\mathbf{s}_i, \mathbf{s}_j; \boldsymbol{\theta}_\gamma)]_{i,j=1}^m$ where $\boldsymbol{\theta}_\gamma$ represents the covariance parameters. The first layer of the hierarchical model structure is:

$$(Y(\mathbf{s}_1, t), \dots, Y(\mathbf{s}_m, t)) \sim Gcop_m[\Sigma; \{\mu(\mathbf{s}), \sigma(\mathbf{s}), \xi(\mathbf{s})\}] \tag{2.1}$$

$$Y(\mathbf{s}, t) \sim \text{GEV}[\mu(\mathbf{s}), \sigma(\mathbf{s}), \xi(\mathbf{s})] \tag{2.2}$$

where $Y(\mathbf{s}, t)$ is the response at site $\mathbf{s}$ and time t and $Gcop_m$ stands for "m-dimensional Gaussian elliptical copula" with dependence matrix Σ. The spatial data layer processes in each year are

assumed independent and identically distributed. Alternatives to using a copula to construct the joint distribution are an assumption of conditional independence [*Cooley et al.*, 2007] and max-stability [*Smith*, 1990; *Schlather*, 2002; *Cooley et al.*, 2006; *Shang et al.*, 2011; *Padoan et al.*, 2010; *Sang*, 2015]. Marginally, observations are assumed to have a generalized extreme value (GEV) distribution.

The second layer of the hierarchy, also known as the process layer, involves spatial models for the GEV parameters

$$\mu(\mathbf{s}) = \beta_{\mu,0} + \mathbf{x}_\mu^T(\mathbf{s})\boldsymbol{\beta}_\mu(\mathbf{s}) + w_\mu(\mathbf{s}) \tag{2.3}$$

$$\sigma(\mathbf{s}) = \beta_{\sigma,0} + \mathbf{x}_\sigma^T(\mathbf{s})\boldsymbol{\beta}_\sigma(\mathbf{s}) + w_\sigma(\mathbf{s}) \tag{2.4}$$

$$\xi(\mathbf{s}) = \beta_{\xi,0} + \mathbf{x}_\xi^T(\mathbf{s})\boldsymbol{\beta}_\xi(\mathbf{s}) + w_\xi(\mathbf{s}) \tag{2.5}$$

where $\beta_{\gamma,0}$ are spatially independent intercept terms, $\mathbf{x}_\gamma^T(\mathbf{s}_i)$ is a vector of p spatially varying predictors and $\boldsymbol{\beta}_\gamma(\mathbf{s})$ is a vector of p spatially varying regression coefficients. Covariates will be discussed in Section 3.2.7.

The shape parameter ξ is notoriously difficult to estimate, its value determining the support of the GEV distribution. Positive values of ξ indicate a lower bound to the distribution, negative values indicate an upper bound and zero indicates no bounds. In many studies, ξ is modeled as a single value per study area or per region within the study area [*Cooley et al.*, 2007; *Renard*, 2011; *Atyeo and Walshaw*, 2012; *Apputhurai and Stephenson*, 2013]. As in [*Cooley and Sain*, 2010], we cannot assume that this parameter is constant over the large study region and so it is modeled spatially along with the other GEV parameters.

For large regions we cannot assume that a constant spatial regression holds for the entire domain and thus must introduce spatial variation in the regression coefficients. The third layer of

the hierarchy involves a spatial model for these regression coefficients

$$\beta_\mu(\mathbf{s}) = \sum_{i=1}^k c_i^\mu \eta_i^\mu(\mathbf{s}) \tag{2.6}$$

$$\beta_\sigma(\mathbf{s}) = \sum_{i=1}^k c_i^\sigma \eta_i^\sigma(\mathbf{s}) \tag{2.7}$$

$$\beta_\xi(\mathbf{s}) = \sum_{i=1}^k c_i^\xi \eta_i^\xi(\mathbf{s}) \tag{2.8}$$

where the c_i's are weights for k basis functions, the η_i's, which are distributed throughout the domain. More details are given in section 2.2.2.

2.2.1 Elliptical copula for data dependence

Elliptical copulas are a flexible tool for modeling multivariate data [*Renard*, 2011; *Sang and Gelfand*, 2010; *Ghosh and Mallick*, 2011; *Renard and Lang*, 2007]. This class of copulas can represent spatial data with any marginal distribution, a particularly attractive feature for extremal data. The Gaussian copula constructs the joint pdf of a random vector $(Y_1, ... Y_m)$ as

$$F_{Gaussian}(y_1, \ldots, y_m) = \Phi_\Sigma(u_1, ... u_m) \tag{2.9}$$

where $\Phi_\Sigma(u_1, ... u_m)$ is the joint cdf of an m-dimensional multivariate normal distribution with covariance matrix Σ, $u_i = \phi^{-1}(F_i[y_i])$, ϕ is the cdf of the standard normal distribution and F_i is the marginal GEV cdf at site i. The corresponding joint pdf is

$$f_{Gaussian}(y_1, \ldots, y_m) = \frac{\prod_{i=1}^m f_i[y_i]}{\prod_{i=1}^m \psi[u_i]} \Psi_\Sigma(u_1, ... u_m) \tag{2.10}$$

where f_i is the marginal GEV pdf at site i, ψ is the standard normal pdf and Φ_Σ is the joint pdf of an m-dimensional multivariate normal distribution.

The dependence between sites is assumed to be a function of distance [*Renard*, 2011]. The dependence matrix is constructed with a simple exponential model

$$\Sigma(i,j) = \exp(-||\mathbf{s}_i - \mathbf{s}_j||/a_0) \tag{2.11}$$

where a_0 is the copula range parameter. Note that the values in this dependence matrix are not covariances, so by analogy with the variogram, the dependence model is termed the dependogram [*Renard*, 2011].

2.2.2   Spatial regression model

For large regions, spatial regression relationships may not hold constant for the entire domain. In this case it is necessary to allow for spatial variation in the spatial regressions for each GEV parameter. Each regression coefficient is represented as a weighted sum of radial basis functions basis functions (Equations 2.6-2.8). The form of these basis functions are

$$\eta_i(\mathbf{s}) = \exp\left(-||\mathbf{s} - \mathbf{s}_i||^2/a_i^2\right) \tag{2.12}$$

where a_i^2 is a range parameter determining the spatial extent of the basis function. These basis functions, also known as Gaussian kernels, are placed at points throughout the domain, known as knots, allowing the regression coefficients to vary smoothly in space.

The knots are placed according to a space-filling design [*Johnson et al.*, 1990; *Nychka and Saltzman*, 1998]. For each GEV parameter, we use 10 knots (Figure 2.1) since based on the author's experience, regression relationships in the western US region tend to hold for regions of a few square degrees. For simplicity, the same knot locations were used for each GEV parameter and the copula but this is not required.
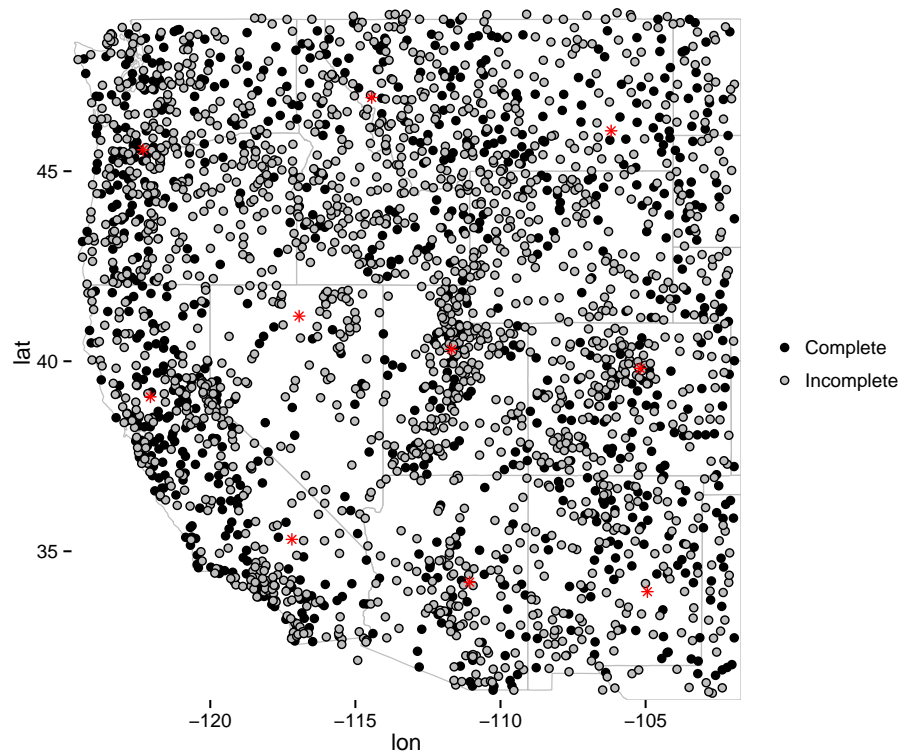
Figure 2.1: Station locations with complete data (black solid dots) and station locations with incomplete data (grey filled dots). Red asterisks are knot locations for the spatially varying regression coefficients.

2.2.3 Missing Data

Stations with missing data can be easily incorporated in the model. When the GEV likelihood is computed, years with missing data are simply skipped. With at least 30 years of data at each station, the GEV parameters can be estimated adequately based on only the available data. For simplicity, the copula was fit to only stations with complete data, though missing data could be incorporated by varying the size of the covariance matrix for each year.

2.2.4 Likelihood and priors

The marginal distribution of $Y(\mathbf{s}_i, t)$ is $\text{GEV}(y(\mathbf{s}_i, t) | \mu(\mathbf{s}_i), \sigma(\mathbf{s}_i), \xi(\mathbf{s}_i))$ where the log-likelihood for some data point y is:

$$\log \text{GEV}(y|\mu, \sigma, \xi) = -\log(\sigma) - (1 + 1/\xi) \log(b) - b^{-1/\xi} \tag{2.13}$$

where $b = 1 + \xi(y - \mu)/\sigma$.

Let γ represent any of the GEV parameters (μ, σ, ξ). The residual Gaussian processes likelihood $p(\mathbf{w}_\gamma | \boldsymbol{\theta}_\gamma)$ is obtained from the multivariate normal density function $\mathbf{w}_\gamma | \boldsymbol{\theta}_\gamma \sim \text{MVN}(\mathbf{0}, \Sigma_\gamma)$, where $\Sigma_\gamma = C(\boldsymbol{\theta}_\gamma)$. We use an exponential covariance function with parameters δ_γ^2 (the partial sill or marginal variance), a_γ (the range) and τ_γ^2 (the nugget), so $\boldsymbol{\theta}_\gamma = (\delta_\gamma^2, a_\gamma, \tau_\gamma^2)$. The parametric form of the covariance function is

$$C(\mathbf{s}_i, \mathbf{s}_j; \boldsymbol{\theta}_\gamma) = \begin{cases} \delta_\gamma^2 \exp(-||\mathbf{s}_i - \mathbf{s}_j||/a_\gamma) & i \neq j \\ \delta_\gamma^2 + \tau_\gamma^2 & i = j \end{cases}$$

We use weakly informative normal priors centered at 0, with a standard deviations as follows: 0.1 $(\delta_\xi^2, \tau_\xi^2)$, 1 $(\delta_\mu^2, \delta_\sigma^2, \tau_\mu^2, \tau_\sigma^2, \beta_0^\xi, c_i^\mu, c_i^\sigma, c_i^\xi; i = 1, \ldots, n)$, 10 $(\beta_0^\mu, \beta_0^\sigma)$, 1000 $(a_\mu, a_\sigma, a_\xi, a_0, a_i; i = 1, \ldots, n)$. For ξ we restrict values to the range $[-0.5, 0.5]$, motivated by the typical ranges seen in precipitation data [*Cooley and Sain*, 2010].

2.3 Estimation

2.3.1 Composite likelihood

Composite likelihood for spatial data is a method in which the full likelihood is approximated by a set of conditional or marginal likelihoods; see *Varin et al.* [2011] for a recent review. Conditional approaches construct the composite likelihood as a product of conditional likelihoods for each observation given neighboring observations [*Vecchia*, 1988; *Stein et al.*, 2004]. Marginal

approaches construct the conditional likelihood as a product of joint densities of groups of observations of two or more. The case when a group consists of one observation is known as the independence likelihood, which precludes the computation of spatial dependence parameters [*Varin et al.*, 2011]. Composite likelihood methods have also been applied to max-stable spatial processes; see *Sang* [2015] for a recent review.

In our approach, the stations are broken up into G groups each with n_g stations. The marginal composite likelihood estimator (L_c) is constructed as a product of the group likelihoods

$$L_c(\boldsymbol{\theta}|\mathbf{y}_1, \ldots, \mathbf{y}_G) = \prod_{g=1}^{G} L_g(\boldsymbol{\theta}|\mathbf{y}_g) \tag{2.14}$$

where $\boldsymbol{\theta}$ contains covariance parameters and $\mathbf{y}_g$ contains observations from group g. This approach is similar to the "small blocks" approach from *Caragea and Smith* [2006, 2007]. Approximating the likelihood in this way requires $O(Gn_g^3)$ computations as opposed to $O(n^3)$. An assumption in this approach is that each group is independent, which is expected to introduce some loss of statistical efficiency. As n_g increases (and G decreases) the composite likelihood estimator approaches the true likelihood at the cost of increased computation time [*Caragea and Smith*, 2007]. The choice of n_g must be a balance between computation time and accuracy. Along these lines, *Caragea and Smith* [2007] suggest that computational efficiency is maximized when n_g is between $m^{1/2}$ and $m^{2/3}$, where m is the total number of stations. In this application, the composite likelihood approximation is applied to compute the copula likelihood as well as each of the latent GEV parameter residuals.

2.3.2 Composite likelihood group size and distribution

In order to use a composite likelihood approach we must decide how many stations to use in each group (n_g). The number of stations in each group should be small enough so as not to incur substantial computational cost but large enough so that the covariance parameters can be adequately estimated. We used 30 stations per group or approximately 1% of the total number of

stations. The consequences of this choice are explored in Section 2.5.2.

We must also choose how stations are to be grouped. Several approaches come to mind such as selecting groups based on climatological regions, elevation bands or a course grid. We chose to group stations randomly, expecting that groups will have a mixture of stations with a range of spatial proximities, allowing for estimation of both small and large scale behavior.

What remains in the model are a few application specific details: selection of the knot locations and the selection of covariates. These are described in the next sections.

2.4   Application to the Western US

2.4.1   Precipitation Data

Daily precipitation data was obtained from the Global Historical Climatology Network (GHCN). We use all available stations in the western US which contain more than 30 years of data from 1950-2013. 3-day maxima were computed fall (SON). For a season to be included for a particular year, we require no more than 25% of the days be missing. The number of stations included (with the number of complete stations in parentheses) was 2618 (848). Figure 2.1 shows the station locations, with solid black points indicating stations with complete data and filled grey points indicating stations with incomplete data. Red asterisks indicate the centers (knots) for the radial basis functions.

2.4.2   Covariates

For all GEV parameters the same covariates are used, i.e., $\mathbf{x}_\mu(\mathbf{s}) = \mathbf{x}_\sigma(\mathbf{s}) = \mathbf{x}_\xi(\mathbf{s}) = \mathbf{x}(\mathbf{s})$. The covariates are elevation and mean seasonal precipitation. Typically, latitude and longitude are used as well but the spatially variation of the regression coefficients precludes this. Covariates were obtained at knot locations, station locations and at a 1/8th degree grid throughout the study area. Elevation data was obtained from the NASA Land Data Assimilation Systems (NLDAS)

website [1] [*Xia et al.*, 2012a, b]. Mean seasonal precipitation was computed from the Maurer dataset [*Maurer et al.*, 2002].

2.4.3 Implementation

The model was implemented in the Stan modeling language [*Stan Development Team*, 2015b] using the RStan interface [*Stan Development Team*, 2015a]. Stan uses the No-U-Turn Sampler (NUTS), an implementation of Hamiltonian Monte Carlo (HMC) [*Betancourt*, 2013; *Hoffman and Gelman*, 2014]. The NUTS sampler deals well with highly correlated parameters, tends to need very few warmup iterations and typically produces nearly uncorrelated samples. For these reasons, very long chains are usually not needed, nor is thinning. The tradeoff in using the NUTS sampler in this application was much longer computation time per sample compared to a traditional Metropolis-Hastings or Gibbs sampler.

Three chains of length 3,000 were run, with the first 1000 iterations discarded as warmup, resulting in 6,000 samples for each parameter in each season. To assess convergence, we compute the $\hat{R}$ statistic to ensure it is below 1.1, as well as visually inspect trace plots.

2.4.4 Computation of gridded return levels

After computing $\mu = [\mu_i]_{i=1}^n$, $\sigma = [\sigma_i]_{i=1}^n$ and $\xi = [\xi_i]_{i=1}^n$ distributions of each GEV parameter are obtained at each 1/8th degree grid cell via conditional simulation. The gridded parameter values are used to compute return levels at each grid cell using the GEV return level formula

$$z_i(r) = \mu_i + \sigma_i((-\log(1 - 1/r))^{-\xi_i} - 1)/\xi_i,$$

where r is the return period in years (100 years for example).

---

[1] http://ldas.gsfc.nasa.gov/nldas/NLDASelevation.php

2.5   Results

2.5.1   Testing the validity of the Gaussian copula

An implication of the Gaussian copula is that marginal distributions are asymptotically independent, or $P(F_x(X) > p | F_y(Y) > p) \to 0$ as $p \to 1$ [*Renard and Lang*, 2007]. To test this we conducted asymptotic independence tests [*Reiss and Thomas*, 2007] for all pairs of stations. The null hypothesis of this test is dependence, so setting a significance level of 99% ensures that stations passing the test exhibit strong asymtotic dependence. At the 99% significance level, 0.15% of pairwise stations exhibited dependence, less that the 1% expected from chance. In addition we examined plots of the station locations when dependence was indicted by the test. These plots did not show any discernible spatial pattern of dependence, for example dependent stations did not tend to fall near each other.

2.5.2   Group size selection

To demonstrate that the selection of group size has little effect on return levels, a small experiment is conducted. We run the model for a region encompassing most of the state of Oregon, using 4 knots. The group size is set to be 2, 5, 10, 15, 20 and 30 stations representing approximately 1%, 2%, 4%, 6%, 8% and 13% of the total number of stations respectively. The same 240 stations (60 complete, 180 incomplete) are used in each model run.

Figure 2.2 shows the median return level for each model run. The results are nearly identical for this range of group sizes, indicating that median return levels are not sensitive to the choice of group size. Credible intervals of return levels (not shown) were quite similar as well, with credible intervals decreasing as group size is increased indicating that a larger group size yields more accurate results, as expected. In light of this we chose a group size of 30 for the large domain which provides both a diversity in the distribution of stations within a group but is small enough to not significantly hider computation.
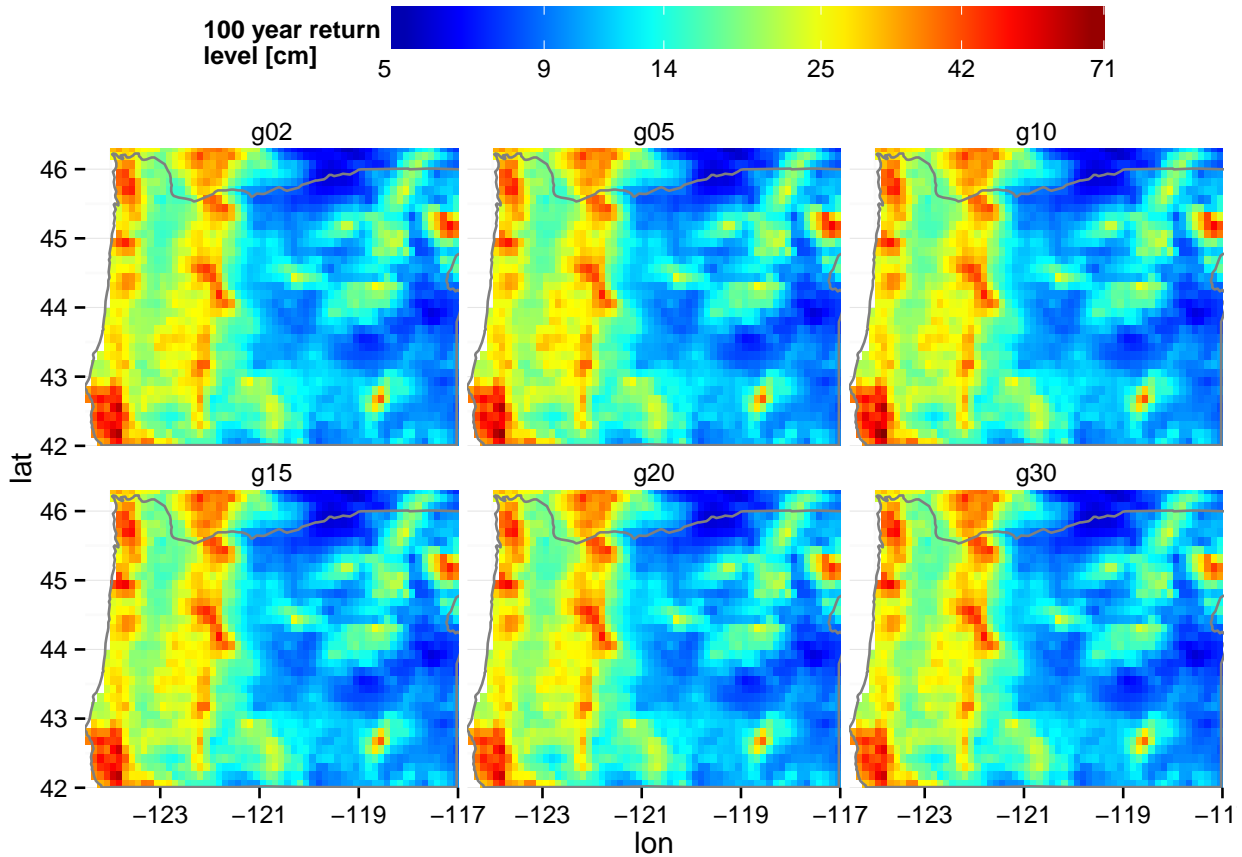
Figure 2.2: Median return levels using a group sizes of 2, 5, 10, 15, 20 and 30. Note the logarithmic color scale.

2.5.3   Gridded return levels

Figure 2.3 shows the median of the GEV parameters after interpolation by conditional simulation. The location and shape fields are highly correlated; locations with higher average extreme precipitation tend to have more variability in these extremes. Values of ξ are always positive, indicating a heavy upper tail. The southern coastal region in California in the summer indicates a very heavy upper tail.

Figure 2.4 shows median return levels and associated uncertainty. Uncertainty tends to be higher in high elevation regions, likely due to the correlation of the location and shape parameters. These results demonstrate the feasibility of the proposed model.
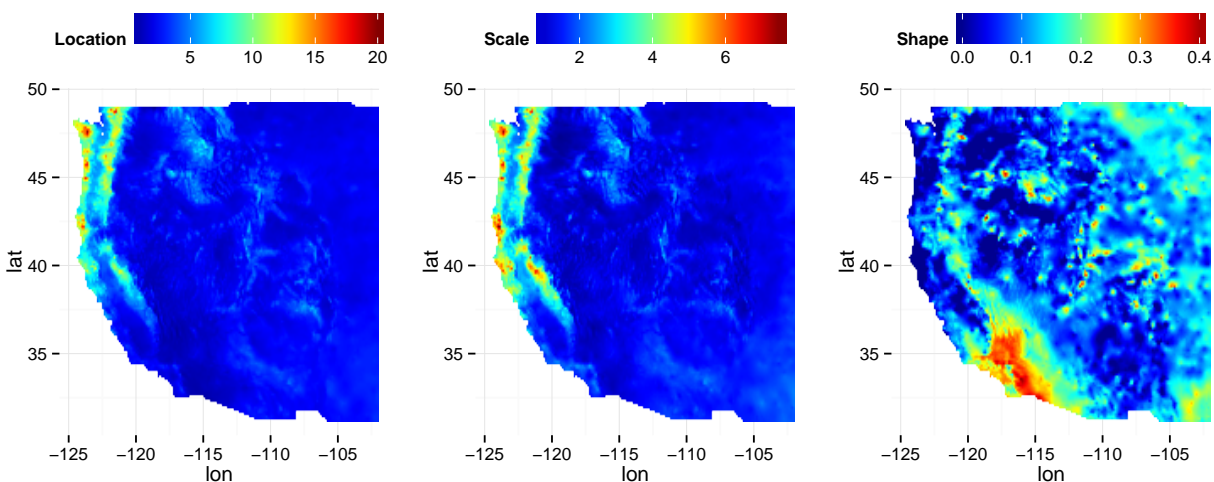
Figure 2.3: Median of underlying GEV parameters, location (μ), scale (σ) and shape (ξ).
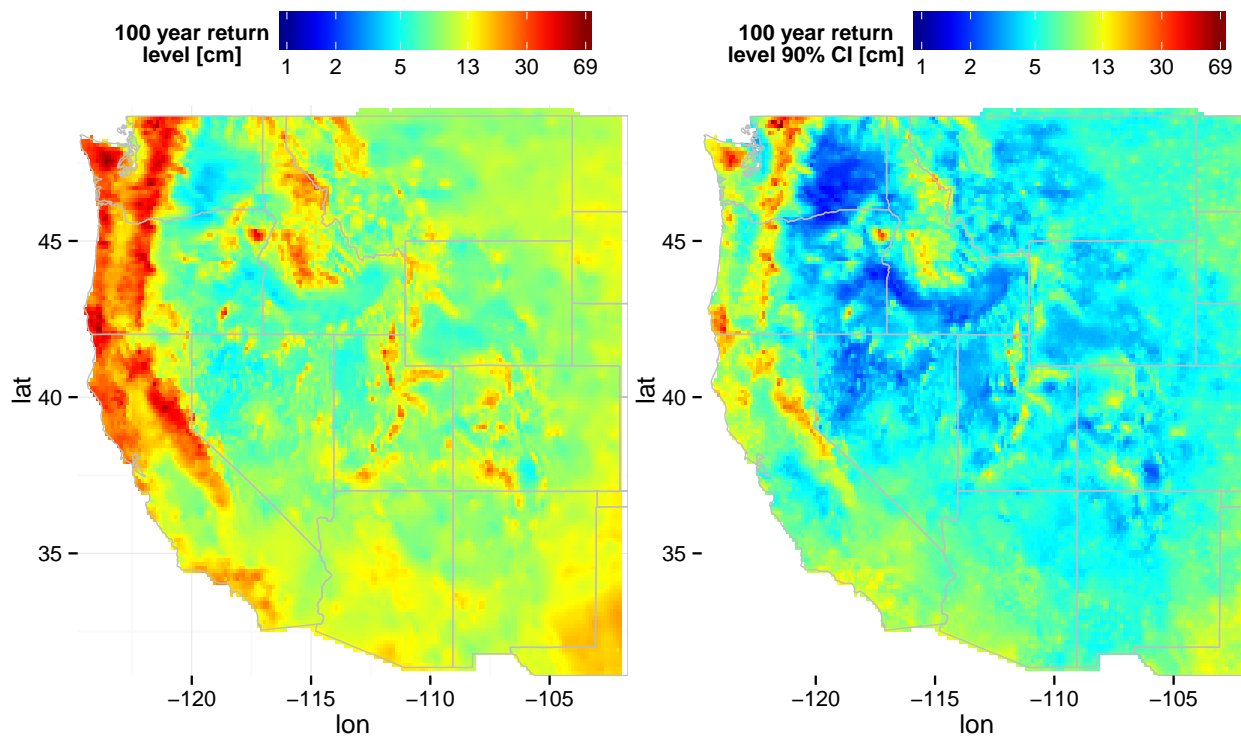
Figure 2.4: Median 100-year return levels for fall (left) and width of corresponding 95% credible interval (right). Note the logarithmic color scale.

2.5.4   Validation

Cross validation was conducted by dropping 885 stations or approximately 35% of the total stations. Gridded return levels were computed for this subset of data. Figure 2.5 shows the difference between the median return level for the full data and subset data. The difference map shows some spatial coherence but none that indicates any strong bias in a single region (states for example). The largest differences occur in areas in the northwest where influential stations were dropped randomly.
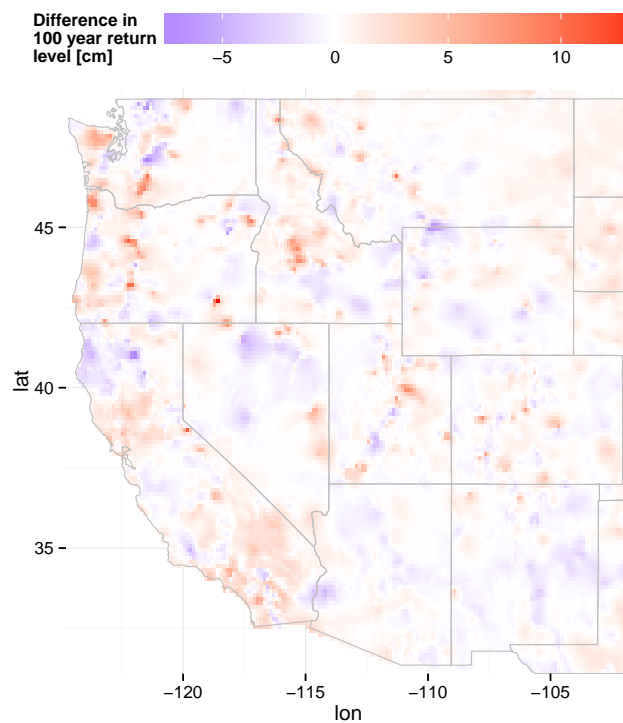
Figure 2.5: Difference between 50th percentile return levels from the full model and the validation model dropping 35% of the data.

2.5.5   A case for composite likelihood

To highlight the usefulness of the composite likelihood approach for this application we present results using a Gaussian predictive process (GPP) model [*Banerjee et al.*, 2008] for the latent GEV parameter processes (Figure 2.6). A Gaussian predictive process model approximates

the likelihood at a small set of knots to reduce the dimension of the covariance matrix and the computational burden of inverting it. We originally set out using GPPs for this application but switched to a composite likelihood approach when we realized the uncertainty was unacceptably large away from knot locations.
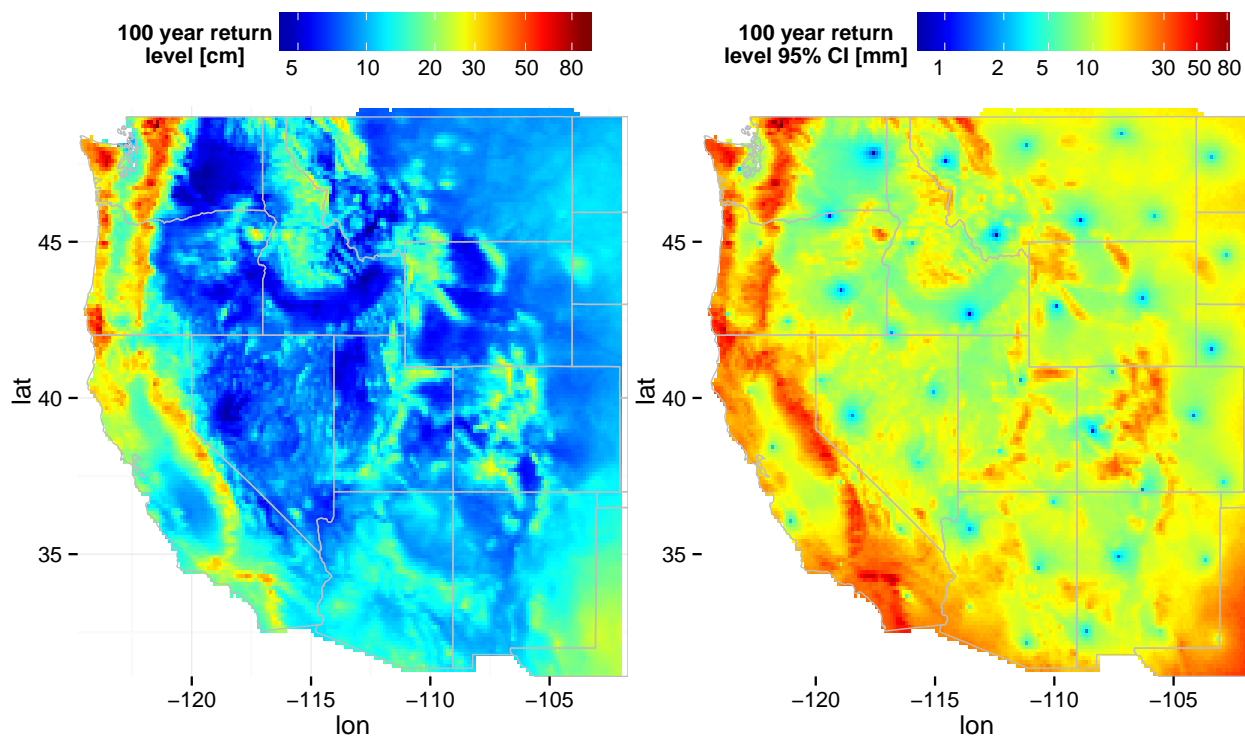
Figure 2.6: Return levels maps produced using latent gaussian predictive processes.

The median return levels with the GPP approach were nearly identical to those from the composite likelihood method (Figure 2.4) but large differences are apparent when looking at the credible intervals of the return levels. Clear artifacts are present at the locations of knots, where uncertainty is greatly reduced. Uncertainty away from knot locations is typically large, rendering this method much less useful than the composite likelihood approach.

2.6   Discussion and conclusions

We describe a general Bayesian hierarchical model for extreme data observed over space and time. The data is assumed to originate from a Gaussian elliptical copula having generalized extreme value (GEV) marginal distributions. Spatial dependence is further captured by Gaussian processes on the three GEV parameters (location, scale and shape). Using a composite likelihood approach, we are able to incorporate 2595 observation locations with 54 years of data. With spatially varying regression coefficients, the model can be applied to arbitrarily large regions. The model was applied to extreme 3-day precipitation in fall in the western United States, a climatologically and geographically diverse region. The model was fit using a standard Bayesian methodology, implicitly capturing uncertainty in the parameter estimates and spatial predictions.

In Section 2.5.5 we briefly examine results for the same region using a Gaussian predictive process (GPP) model for the latent GEV parameters. In this application, GPPs produced unreasonably large posterior credible intervals when moving away from knot locations. In light of this we recommend a composite likelihood approach for regions of equal or larger size than the western US.

A crux of this model is the use of appropriate spatial covariates. Mean seasonal precipitation (MSP) had a correlation of 95% with the MLE estimates of μ and 75% with the MLE estimates of σ. Even with spatially varying regression coefficients, appropriate covariates are key. The covariates here helped in generating realistic spatial variability and helped to reveal a complex spatial pattern for the shape parameter, ξ. The strongest covariate for ξ was elevation. The spatial variability in ξ shows that it is inappropriate to model without spatial variation for anything but the smallest regions.

A number of extensions can be made to this framework. The most obvious extension is to allow temporal variation in the GEV parameters by including temporal covariates. While this extension remains infeasible for the size of the current study region, it may be feasible for smaller regions, say a single state or moderate sized river basin. Additional spatial covariates could be

included; for example, seasonal temperature, winds or evapo-transpiration. A model such as the one presented here can be used to investigate changes in risk under specific climate regimes (i.e. ENSO); one would simply include the mean seasonal precipitation field from strong El Niño or La Niña years. Because we incorporate a data layer, this model could be used to simulate realistic fields of extremes under specific climate regimes. Finally, we plan to explore the linking of streamflow data into the hierarchy, so that streamflow extremes can be simultaneously estimated.

Acknowledgments

Pre- and postprocesseing analysis was conducted using the R language [*R Core Team*, 2014].

Data is available at: `http://bechtel.colorado.edu/~bracken/spatial_extremes/data/`.

Chapter 3

A Bayesian hierarchical approach for joint nonstationary regional frequency analysis of precipitation and streamflow extremes

Abstract

We present a Bayesian hierarchical model for conducting joint nonstationary regional frequency analysis of precipitation and streamflow extremes, which are linked to large scale climate forcings. The extremes of precipitation and streamflow are modeled as Generalized Extreme Value (GEV) distribution with parameters varying in time and both time and space for precipitation. Specifically, Temporal nonstationary is captured by including several large scale climate indices as covariates and multivariate dependence between variables is captured with a Gaussian elliptical copula. Precipitation and streamflow are coupled at the data and process levels of the hierarchy. Furthermore, the parameters of the precipitation extremes are included as covariates for obtaining the streamflow parameters, this coupling provides for the data to lend strength in space and time. Through exploratory data analysis, we identified a basin from several candidate basins in western US for which linking streamflow and precipitation frequency analysis is appropriate, typically rainfall-runoff dominated. The candidate basin selected was United States Geological Survey (USGS) gage 11098000, in southern California, for which the model was applied. Results indicated that the uncertainty in regional streamflow return levels were greatly reduced by the coupling of precipitation and streamflow in the parameter and data levels. Furthermore, the multivariate dependence helped to capture the joint relationship between precipitation and streamflow extremes very well, compared to the independent version of the model.

3.1   Introduction

There is increasing evidence for temporal nonstationarity of streamflow and precipitation extremes in the Western US [*Bracken et al.*, 2015; *Kunkel et al.*, 2003; *Groisman et al.*, 2001; *Kunkel et al.*, 1999; *Cayan et al.*, 1999], both as trends in time and modulation from large scale atmospheric oscillations such as the Atlantic Multidecadal Oscillation (AMO), the Pacific Decadal Oscillation (PDO) and the El Nio Oscillation (ENSO). Nonstationarity in extremes at individual locations typically involves modeling the underlying distribution parameters as a function of covariates including time. Semi-parametric and nonparametric approaches have been proposed with applications to flow extremes [*Sankarasubramanian and Lall*, 2003; *Apipattanavis et al.*, 2010]. Modeling nonstationarity using GEV [*Coles*, 2001; *Katz*, 2010] have become popular in applications to flow and precipitation extremes [*Towler et al.*, 2009]. Extension of these within in a Bayesian framework to accurately capture the uncertainties have been made to model precipitation extremes [*Apputhurai and Stephenson*, 2013; *Ghosh and Mallick*, 2011; *Sang and Gelfand*, 2009a] and streamflow extremes [*Najafi and Moradkhani*, 2014; *Renard and Lang*, 2007; *Najafi and Moradkhani*, 2013; *Yan and Moradkhani*, 2014]. The frequency analysis of precipitation and streamflow extremes described above are typically conducted separately.

This analysis is inherently data limited as extreme events are rare occurrences. One method for addressing this issue is known as regional frequency analysis (RFA). RFA is a well-known approach in hydrology for analyzing extremes where observations from multiple locations are assumed to follow the same probability distribution [*Hosking and Wallis*, 1993] but with the distribution parameters varying in space. RFA is composed of three main steps, (1) delineation of a homogeneous region, (2) fitting a regional probability distribution i.e., developing relationship between model parameters and spatial attributes such as watershed area, slope etc., and (3) transferring information to ungaged sites. Several recent studies have proposed improvements and extensions using Bayesian framework to this approach which allow for climatic nonstationarity [*Renard and Lall*, 2014] and obviate the delineation of homogeneous regions [*Cooley et al.*, 2007;

Bracken et al., 2016]. Bayesian approaches allow for robust estimation of uncertainties which are not easily accomplished with traditional RFA.

When spatial data is available, RFA is robust and easy to implement but in data limited regions, RFA may not be possible. In these situations, when we must resort to a single-site approach, nonstationary frequency analysis may not be possible due to model convergence issues, large uncertainties in parameter estimates, etc. [*Serinaldi and Kilsby*, 2015]. It is reasonable to assume, especially in rainfall-runoff dominated regions, that annual or seasonal maximum precipitation and streamflow are closely related which motivates a multivariate analysis.

Multivariate frequency analysis improves upon RFA by explicitly capturing the dependence between multiple hydrologic variables such as precipitation and streamflow. Dependence is typically captured by specifying a joint distribution for two or more variables. *Favre et al.* [2004] used a variety of copulas to capture the joint distribution of peak flows at two locations on a river network. *Chebana and Ouarda* [2011] specify a joint distribution for the quantiles of peak flow and volume using a copula. *Yue and Rasmussen* [2002], *Kao and Govindaraju* [2007] and *Vandenberghe et al.* [2011] conduct bivariate frequency analysis of rainfall and streamflow extremes using copulas.

In this study we propose a Bayesian hierarchical approach for joint nonstationary regional frequency analysis of streamflow and precipitation extremes. This study is motivated by the need for alternatives to RFA in data limited regions where multiple hydrologic variables are available with known links to large scale climate. We demonstrate the utility of the approach with an application to a rainfall-runoff watershed in the southwestern US. The results of the joint model are compared to an independent model where distributions are fit to streamflow and precipitation independently. The methodology is first described along with the priors, fitting procedure and, estimation of the nonstationary return levels. The exploratory analysis proposed to identify a candidate watershed is then described along with the selected covariates. Results from the model providing nonstationary frequency estimates are presented, followed by conclusions and discussions.

3.2   Methodology

3.2.1   GEV frequency analysis

Frequency analysis of hydrologic timeseries is generally performed on block i.e., seasonal or annual, extremes. Theory dictates, such block extremes follow a generalized extreme value (GEV) distribution [*Coles*, 2001]. The three parameter GEV cumulative distribution is

$$F(y; \mu, \sigma, \xi) = \exp\left\{ - \left[1 + \xi \left(\frac{y - \mu}{\sigma} \right) \right]^{-1/\xi} \right\} \tag{3.1}$$

where μ, σ, and ξ are known as the location, scale, shape parameters, respectively. The shape parameter controls the support of the distribution with $\xi < 0$ implying an upper bound, $\xi > 0$ implying a lower bound, and $\xi = 0$ implying support on the whole real line. In a GEV-based frequency analysis, a GEV distribution is fit to block maxima data and the desired upper tail quantiles, known as return levels, are estimated.

In a stationary GEV analysis, the distribution parameters are assumed to be constant in time, while in a nonstationary GEV analysis models parameters are allowed to vary in time as a function of covariates or time trends [*Coles*, 2001; *Katz*, 2010]. They are typically a linear model of the covariates, for example, allowing a liner trend and one covariate in the location parameter, a single site nonstationary GEV model would be

$$y(t) \sim GEV(\mu(t), \sigma(t), \xi(t)) \tag{3.2}$$

$$\mu(t) = \mu_0 + \mu_1 t + \mu_2 x(t) \tag{3.3}$$

$$\sigma(t) = \sigma_0 \tag{3.4}$$

$$\xi(t) = \xi_0 \tag{3.5}$$

where $x(t)$ is a covariate, perhaps a large scale climate index.

In general, streamflow and precipitation extremes are driven by the same large scale climate drivers, so the parameters of their respective GEV distribution are expected to be related, in addi-

tion to the joint relationship between the data themselves. We exploit this inherent relationship in our model structure described below.

3.2.2 Exploratory analysis

In this exploratory analysis, we selected unimpaired basins from the Newman dataset [*Newman et al.*, 2014, 2015] dataset and precipitation gages from the Global Historical Climatology Network (GHCN) [*Menne et al.*, 2012]. The analysis steps were:

(1) For both precipitation and flow, 3-day winter maxima were computed from daily data which implies that the data follow a GEV distribution [*Coles*, 2001].

(2) Basins were included with at least 10 precipitation gages within $0.5°$ of the basin outlet and at least 30 years of complete data.

(3) Nonstationary GEV models were then fit to precipitation and streamflow independently with maximum likelihood estimation (MLE) using identical climate covariates (covariates are discussed in Section 3.2.7).

(4) Correlations between the nonstationary parameter estimates were then computed, with strong correlations indicating a linear relationship is appropriate (Figure 3.2).

Basins on the coast of California stood out with strong and positive correlations with the nonstationary location parameters from the nearby flow gage. No candidate basins exhibited uniform relationships for the scale and shape parameters. The basin in southwest (USGS gage 11098000) was selected for further analysis due to it having the strongest correlations.

These exploratory results indicate that in at least some regions of the western US, assuming a linear relationship between the GEV location parameter is appropriate. This is likely due to the strong influence of the El Niño Southern Oscillation on winter precipitation and streamflow in this region [*Cayan et al.*, 1999].
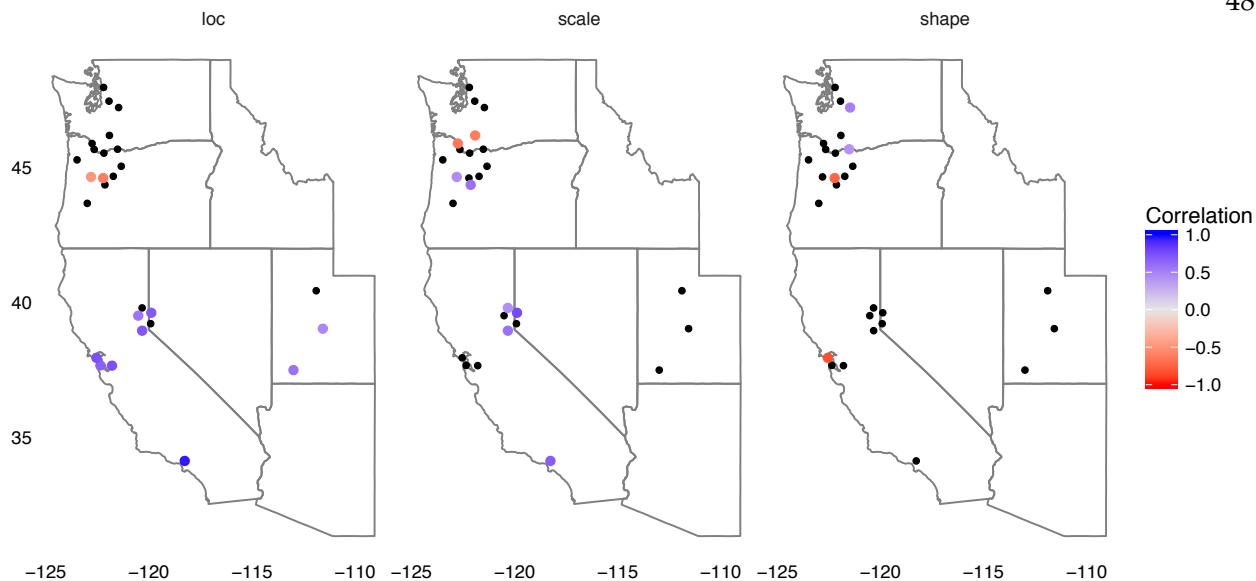
Figure 3.1: Regional mean correlations between nonstationary GEV parameter estimates for peak 3-day total flow with peak 3-day total rainfall from surrounding rain gages. Each point indicates the approximate location of a basin outlet and a colored point indicates the strength of the correlation, with black points indicating no significant relationship.

3.2.3 Joint model structure

Given a candidate basin, USGS gage 11098000 in southern California and 16 surrounding GHCN precipitation gages, we present a model for joint analysis of precipitation and streamflow extremes which takes advantage of the latent GEV parameter relationship justified in the previous section.

Let $y_1(t), \ldots, y_n(t)$ be precipitation timeseries, $z(t)$ be the flow timeseries and $\mathbf{x}(t)^T$ be a vector of climate covariates. The general linked model structure is

$$(y_1(t), ..., y_n(t), z(t)) \sim C_g(\Sigma; \{\mu_y(t), \sigma_y(t), \xi_y, \mu_z(t), \sigma_z(t), \xi_z\}) \tag{3.6}$$

$$y(t) \sim GEV(\mu_y(t), \sigma_y(t), \xi_y) \tag{3.7}$$

$$z(t) \sim GEV(\mu_z(t), \sigma_z(t), \xi_z) \tag{3.8}$$

$$\mu_y(t) = \mu_{y0} + \mathbf{x}(t)^T \beta_\mu \tag{3.9}$$

$$\mu_z(t) = a + b\mu_y(t) \tag{3.10}$$

$$\sigma_y(t) = \sigma_{y0} + \mathbf{x}(t)^T \beta_{\sigma_y} \tag{3.11}$$

$$\sigma_z(t) = \sigma_{z0} + \mathbf{x}(t)^T \beta_{\sigma_z} \tag{3.12}$$

where β_μ, β_{σ_y} and β_{σ_z} are latent regression parameters and a and b are parameters which serve to link the precipitation and flow. C_g represents the Gaussian elliptical copula with dependence matrix Σ, a positive definite matrix whose elements take values between -1 and 1, essentially representing correlations between variables. The diagonal elements of Σ are therefore equal to 1.

In order to capture the spatial dependence between both precipitation and streamflow locations, Σ is decomposed into two dependence models, one for the precipitation locations with themselves, and one for the streamflow location with the precipitation locations. Σ is then constructed

$$\Sigma = \begin{bmatrix} D & \nu \\ \nu & 1 \end{bmatrix} \tag{3.13}$$

We assume the correlation between observation locations decreases exponentially with distance, in which case

$$\nu_i = \exp(||\mathbf{p}' - \mathbf{p}_j||/\phi_1)$$

and

$$D_{ij} = \exp(||\mathbf{p}_i - \mathbf{p}_j||/\phi_2)$$

where $\mathbf{p}'$ is the streamflow coordinate and $\mathbf{p}_i$'s are the precipitation coordinates and ϕ_1 and ϕ_2 are range parameters controlling how quickly correlation decays with distance.

3.2.4 Elliptical copula

A Gaussian elliptical copula is a multivariate probability distribution with pre-specified marginals in which the joint distribution is multivariate normal [*Renard and Lang*, 2007]. Elliptical copulas are useful as a practical tool for multivariate modeling, due to their flexibility and ease of implementation [*Renard*, 2011; *Sang and Gelfand*, 2010; *Ghosh and Mallick*, 2011; *Renard and Lang*, 2007].

Let $\mathbf{V}(t) = (V_1(t), \ldots, V_n(t))$ be a random vector of hydrologic variables at time t and let $\mathbf{v}(t) = (v_1(t), \ldots, v_n(t))$ be a vector of the corresponding realizations. The Gaussian copula constructs the joint cumulative distribution function (cdf) of $\mathbf{V}(t)$ as

$$F_C(\mathbf{v}(t)) = \Phi_\Sigma(\mathbf{u}(t)) \tag{3.14}$$

where $\Phi_\Sigma(\cdot)$ is the joint cdf of an n-dimensional multivariate normal distribution with covariance matrix Σ, $\mathbf{u}(t) = (u_1(t), \ldots, u_n(t))$, $u_i(t) = \phi^{-1}(F_{it}[v_i(t)])$, ϕ^{-1} is the inverse cdf (quantile function) of the standard normal distribution and $F_{it}(\cdot)$ is the marginal GEV cdf of variable i at time t. The corresponding joint pdf is

$$f_C(\mathbf{v}(t)) = \frac{\displaystyle\prod_{i=1}^{n} f_i[v_i(t)]}{\displaystyle\prod_{i=1}^{n} \psi[u_i(t)]} \Psi_\Sigma(\mathbf{u}(t)) \tag{3.15}$$

where $f_{it}(\cdot)$ is the marginal GEV pdf for variable i at time t, $\psi(\cdot)$ is the standard normal pdf and $\Psi_\Sigma(\cdot)$ is the joint pdf of an n-dimensional multivariate normal distribution.

3.2.5 Likelihood

Let $\mathbf{y} = [\mathbf{y}_1, ..., \mathbf{y}_n]$ be a matrix of precipitation observations where $\mathbf{y}_i = [y_i(t)]_{t=1}^T$ is a vector of observations at one site, let $\mathbf{y}(t) = [y_i(t)]_{i=1}^n$ be a vector of all variables at time t, let $\mathbf{z} = [z(t)]_{t=1}^T$ be a vector of streamflow observations, and let $X = [\mathbf{x}_1, \ldots, \mathbf{x}_n]$. If $\boldsymbol{\theta} = [\phi_1, \phi_2, \beta_{\mu_y}, \beta_{\sigma_y}, \beta_{\sigma_z}, \mu_{y0}, \sigma_{y0}, \sigma_{z0}, a, b]$, a vector of all model parameters, then by Bayes' rule, the posterior distribution can be written

$$p(\boldsymbol{\theta}|\mathbf{y}, \mathbf{z}, X) \propto p(\mathbf{y}, \mathbf{z}|\boldsymbol{\theta}, X)p(\boldsymbol{\theta}) \tag{3.16}$$

where the term $p(\mathbf{y}, \mathbf{z}|\boldsymbol{\theta}, X)$ is known as the likelihood and $p(\boldsymbol{\theta})$ is the prior. Assuming temporal independence,

$$p(\mathbf{y}, \mathbf{z}|\boldsymbol{\theta}, X) = \prod_{t=1}^T p(\mathbf{y}(t), z(t)|\boldsymbol{\theta}, X) \tag{3.17}$$

where $p(\mathbf{y}(t), z(t)|\boldsymbol{\theta}, X)$ is given by Equation 4.8 where the GEV likelihood is

$$f_i(y_i(t)|\mu(t), \sigma(t), \xi_i) = \frac{1}{\sigma_i} b_i^{-1/\xi_i - 1} \exp\left(-b_i^{-1/\xi_i}\right) \tag{3.18}$$

where

$$b_i = 1 + \xi_i \left(\frac{y_i(t) - \mu_i(t)}{\sigma_i}\right). \tag{3.19}$$

3.2.6 Exploratory analysis

3.2.7 Covariates

In order to select a suitable watershed to test our model an exploratory analysis is performed. In this, we selected streamflow from unimpaired basins from the Newman dataset [*Newman et al.*, 2014, 2015] and precipitation gages from the Global Historical Climatology Network (GHCN) [*Menne et al.*, 2012].

Winter average indices of the El Niño Southern Oscillation (ENSO), the Pacific Decadal Oscillation (PDO) and the Atlantic Multidecadal Oscillation (AMO) as covariates. We obtained values of the multivariate ENSO index (MEI) [*Wolter and Timlin*, 1998, 1993] from `http://www.esrl.noaa.gov/psd/enso/mei/`. PDO values [*Zhang et al.*, 1997] were obtained from `http://research.jisao.washington.edu/pdo/`. AMO values [*Enfield et al.*, 2001] were obtained from `http://www.esrl.noaa.gov/psd/data/timeseries/AMO/`. The covariate vector is

$$\mathbf{x}(t)^T = [1, \text{MEI}_w(t), \text{PDO}_w(t), \text{AMO}_w(t)] \tag{3.20}$$

The analysis steps were:

(1) For both precipitation and flow, 3-day winter maxima were computed from daily data which implies that the data follow a GEV distribution [*Coles*, 2001].

(2) Basins were included with at least 10 precipitation gages within $0.5°$ of the basin outlet and at least 30 years of complete data.

(3) Nonstationary GEV models were then fit to precipitation and streamflow independently with maximum likelihood estimation (MLE) using identical climate covariates (covariates are discussed in Section 3.2.7).

(4) Correlations between the nonstationary parameter estimates were then computed, with strong correlations indicating a linear relationship is appropriate (Figure 3.2).

Basins on the coast of California stood out with strong and positive correlations with the nonstationary location parameters from the nearby flow gage. No candidate basins exhibited uniform relationships for the scale and shape parameters. The basin in southwest (USGS gage 11098000) was selected for further analysis due to it having the strongest correlations.

These exploratory results indicate that in at least some regions of the western US, assuming a linear relationship between the GEV location parameter is appropriate. This is likely due to the

Figure 3.2: Regional mean correlations between nonstationary GEV parameter estimates for peak 3-day total flow with peak 3-day total rainfall from surrounding rain gages. Each point indicates the approximate location of a basin outlet and a colored point indicates the strength of the correlation, with black points indicating no significant relationship.

strong influence of the El Niño Southern Oscillation on winter precipitation and streamflow in this region [*Cayan et al.*, 1999].

3.2.8   Model fitting and priors

The model was fit with a Monte Carlo Markov chain (MCMC) approach using a univariate slice sampler [*Neal*, 2003] within a Gibbs sampler. We ran 3 chains of 100,000 iterations, discarding the initial 50,000 iterations and keeping every 10 iterations thereafter, for a total 15,000 posterior samples. To assess convergence we inspected trace plots and computed the $\hat{R}$ statistic [*Gelman and Rubin*, 1992] for each parameter, all computed $\hat{R}$ values were less than 1.1, indicating successful convergence.

Uninformative uniform priors were used for all parameters.

3.3   Results

Posterior distribution of the coefficients of climate covariates are shown in Figure 3.3. The covariates being normalized and scaled to unit variance can be compared in terms of strength. The ENSO index is the strongest covariate, having about twice the influence of PDO and AMO, not surprising given the known ENSO influence in the region [*Cayan et al.*, 1999].
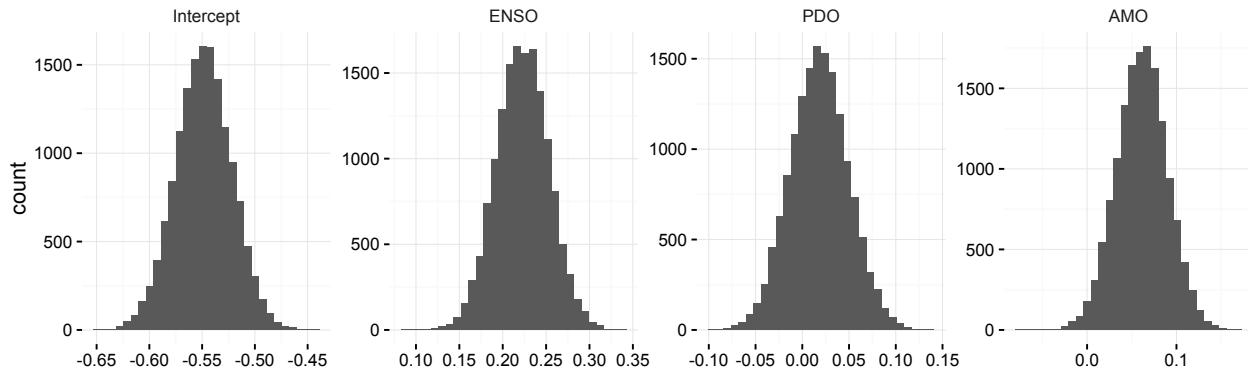
Figure 3.3: Posterior distributions of latent regression coefficients β_μ, plot titles correspond to the coefficients of the covariates.

Nonstationary return levels (GEV quantiles) of precipitation were computed for each posterior sample in each year, from the joint and independent model, which collectively represent the uncertainty in the model parameters given the data – shown as boxplots in Figures 3.4 and 3.5. The return levels from the joint model (Figure 3.4, left) show little difference from the independent model (Figure 3.4, right), though uncertainty is slightly reduced in the joint model. This is not unexpected as the linear coupling between streamflow and precipitation parameters is primarily designed to benefit the streamflow return levels. For streamflow return levels, uncertainty in the joint model (Figure 3.5, left) is greatly reduced compared to the independent model (Figure 3.5, right), a major benefit of the joint model in this application. The reduction in uncertainty in the joint model is due to borrowing of strength from precipitation. Also, the year-to-year variability is quite clear in the joint model.

To compare with the observed flow extremes, median 2-year return levels (i.e. median) are plotted in Figure 3.6. The data are scaled to have mean 0 and standard deviation 1 for comparison
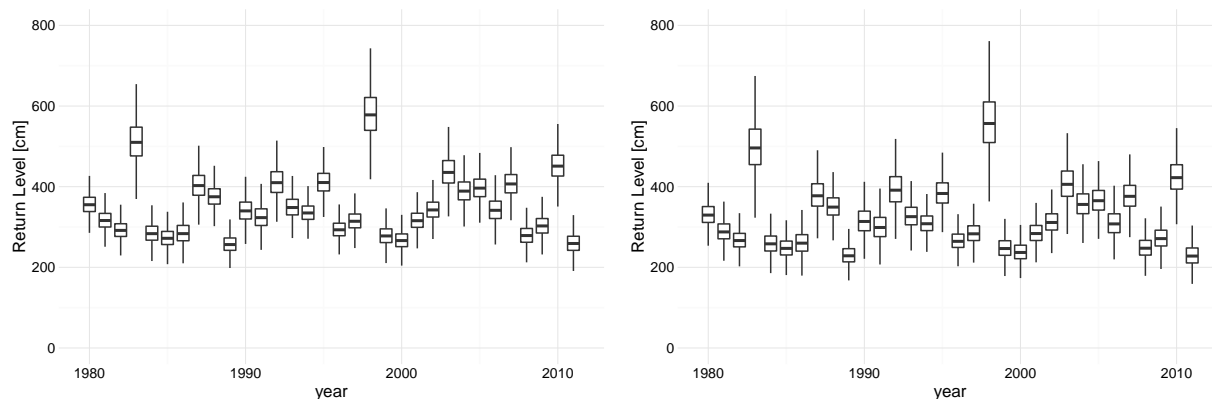
Figure 3.4: Box plots of 100 year return levels of regional precipitation for the joint model (left) and the independent model (right).
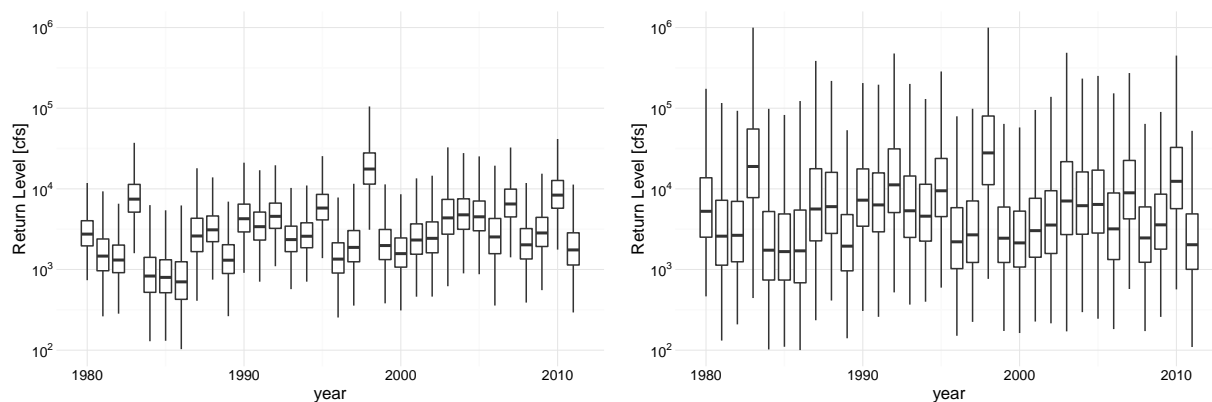
Figure 3.5: Box plots of 100 year return levels of streamflow for the joint model (left) and the independent model (right).

purposes. Since return levels are simply quantiles from the predicted GEV distribution in each year, a direct observed/predicted comparison is not possible but we would expect the timeseries to be correlated, which they are. The predicted return levels are generally high in years with high flow extremes, with the exception of 2005, perhaps due to unaccounted for antecedent conditions.

The dependence structure of the joint model (Figure 3.7, left) more closely represents observations compared to the independent model (Figure 3.7, right), due to the inclusion of the copula. This multivariate dependence is important when simulating extremes for planning, management and mitigation of risks.
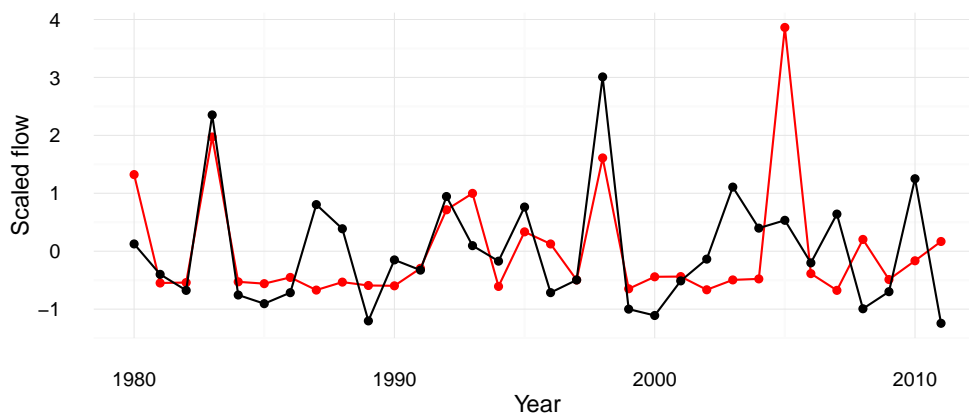
Figure 3.6: Median 2-year return levels (black) plotted with observed flow (red). Both timeseries are scaled to have mean 0 and standard deviation 1
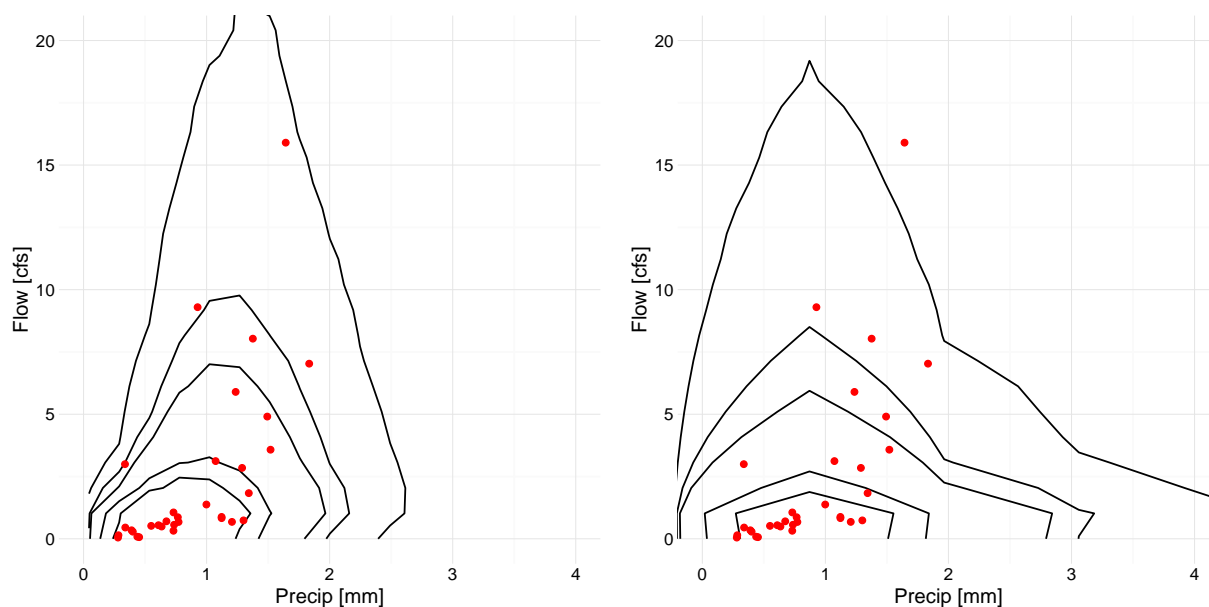
Figure 3.7: Dependence between precipitation and streamflow as simulated by the joint model (left) and the independent model (right) with observed values shown as red points.

3.4   Discussion and conclusions

In this study, we presented a model for joint Bayesian hierarchical nonstationary regional frequency analysis of precipitation and streamflow extremes where nonstationarity was induced by large scale climate covariates. Joint behavior was captured at the data level by a Gaussian el-

liptical copula and at the parameter level by linearly linking the GEV location parameters. This approach is particularly useful for data limited regions as an alternative to RFA. Any number of precipitation and streamflow stations may be included without the need for delineation of homogeneous regions.

We demonstrated two key benefits to conducting frequency analysis in this way:

- Uncertainty was greatly reduced in the estimates of streamflow return levels in the joint model. This is primarily due to the linear linking of the GEV location parameters. In the independent streamflow model, uncertainty was large because 32 data points were used to estimate 9 parameters.

- The multivariate dependence structure of the joint model much more closely matched that of the data indicating than when simulating from independent models, risk may be misrepresented.

By two simple linking mechanisms (copula and latent parameter link) we were able to capture a complex dependence relationship between streamflow and precipitation, indicating that in this application at least, simple linear responses to large scale climate can produce complex nonlinear dependencies. Though we demonstrated this approach with a single streamflow site, the model could be easily modified to allow for multiple flow locations. In this same fashion, the model could be modified to include other atmospheric or hydrologic variables. Spatial covariates and spatial processes on the GEV parameters could also be included to allow for full spatial analysis.

Chapter 4

A Bayesian hierarchical approach to multivariate nonstationary hydrologic frequency analysis

Abstract

We present a Bayesian hierarchical framework for conducting nonstationary frequency analysis of multiple hydrologic variables. In this, marginally, each variable is assumed to follow a Generalized Extreme Value (GEV) distribution in which the location parameter is allowed to vary in time. A Gaussian elliptical copula is used to model the joint distribution of all variables. We demonstrate the utility of this framework with a joint frequency analysis model of annual peak snow water equivalent (SWE), annual peak flow, and annual peak reservoir elevation at Taylor Park dam in Colorado, USA. Indices of large scale climate drivers El Niño Southern Oscillation (ENSO), Pacific Decadal Oscillation (PDO) and Atlantic Multidecadal Oscillation (AMO) are used as covariates to model temporal nonstationarity. The Bayesian framework provides the posterior distribution of the model parameters and consequently the return levels. Results show that performing a joint frequency analysis reduces the uncertainty in return level estimates and better captures multivariate dependence compared to an independent model.

4.1   Introduction

Hydrologic frequency analysis estimates occurrence probabilities of rare hydrologic events by fitting a probability distribution to observed extremes. Quantiles from the fitted distribution give the magnitude of an event associated with a specified non-exceedance probability. The return

level (aka magnitude) associated with a T-year return period is the $(1 - 1/T)$th quantile of the distribution. A number of probability distributions are available to describe the behavior of extremes, the generalized extreme value (GEV) distribution and the generalized pareto distribution (GPD) being consistent with extreme value theory (EVT) [*Coles*, 2001].

Given a daily timeseries of some variable, if the maximum value is selected from a predetermined block of time (annually, say), then the resulting timeseries will follow a three parameter GEV distribution which can describe a wide range of tail behaviors. This approach is called the block maxima method. In the most simple form of block maxima frequency analysis, a stationary GEV distribution is fit to a dataset at a single location, and return levels are computed for a range of return periods. A stationary GEV distribution is one in which the parameters of that distribution are constant in time.

Although the GEV distribution is flexible for modeling flood extremes, the Log Pearson type III (a Gamma distribution fitted to logarithm of the data) is widely used [*Bobée*, 1975; *Bobee and Robitaille*, 1977] and is the legal standard. In this study, however, we focus our attention on the generalized extreme value distribution (GEV) due to its ability to capture a wide range of tail behaviors and its use in previous hydrologic studies [*Najafi and Moradkhani*, 2014; *Davison et al.*, 2012; *Ghosh and Mallick*, 2011; *Renard*, 2011; *Katz*, 2010; *Sang and Gelfand*, 2009b; *Katz et al.*, 2002].

There is growing evidence of the effects of climate change on hydroclimate extremes [*Milly et al.*, 2008; *Katz*, 2010], highlighting the importance of nonstationary analyses. Under the assumption of stationarity, parameters of the GEV distribution are assumed to be constant in time, and consequently return levels are also constant in time. Nonstationary frequency analysis incorporates time varying covariates into the estimates of GEV parameters [*Aryal et al.*, 2009; *Ouarda and El Adlouni*, 2011; *Cheng et al.*, 2014; *Machado et al.*, 2015; *Tan and Gan*, 2015; *Cheng et al.*, 2016]. In a simple nonstationary case, a linear time trend can be incorporated in the GEV paramters [*Cheng et al.*, 2014]. Effects of large scale climate can also be incorporated by including climate covariates such as the El Niño Southern Oscilation (ENSO) and the pacific decadal oscilation (PDO) [*Renard and Lall*, 2014].

Bayesian approaches to fitting GEV models provide several benefits beyond maximum likelihood estimation (MLE) methods. Frequency analyses are typically data limited, and MLE methods may diverge in these situations. In a Bayesian setting, through the use of priors, expert knowledge can be incorporated and model convergence can be improved [*AghaKouchak et al.*, 2013]. Finally, uncertainty is propagated naturally in a Bayesian model without the need for bootstrapping or other ad-hoc uncertainty estimation methods. Inability to converge, or computationally intensive efforts may restrict the use of these methods.

Regional frequency analysis (RFA) is a well known procedure for incorporating observations at multiple locations in a homogeneous region where all the data is assumed to follow the same probability distribution [*Hosking and Wallis*, 1993; *Bradley*, 1998]). By including observations from multiple locations, RFA provides two main benefits over single-site models: (1) frequency estimates at ungauged locations and (2) improved estimates of distribution parameters at all the locations. Recent improvements to regional frequency analysis using a Bayesian hierarchical approach, allow for estimation of streamflow quantiles at ungaged sites [*Chebana et al.*, 2014; *Yan and Moradkhani*, 2014; *Lima et al.*, 2015] precipitation quantiles, [*Bracken et al.*, 2016; *Renard*, 2011], all with attendant uncertainties.

Multivariate frequency analysis improves upon regional frequency analysis by explicitly capturing the dependence between multiple hydrologic variables such as flow at two gages on a network, or two variables measured at the same location, say peak flow and volume. Dependence is typically captured by specifying a joint distribution for two or more variables. *Favre et al.* [2004] used a variety of copulas to capture the joint distribution of peak flows at two locations on a river network. *Chebana and Ouarda* [2011] specify a joint distribution for the quantiles of peak flow and volume using a copula. *Yue and Rasmussen* [2002], *Kao and Govindaraju* [2007] and *Vandenberghe et al.* [2011] conduct bivariate frequency analysis of rainfall and streamflow extremes using copulas. Another form of multivariate frequency analysis is the field of spatial extremes modeling [*Cooley et al.*, 2007; *Bracken et al.*, 2016].

Bayesian approaches have been proposed to conduct nonstationary frequency analysis. *El Ad-*

louni and Ouarda [2009] and *Ouarda and El Adlouni* [2011] conduct simultaneous model selection and parameter estimation of a nonstationary GEV model using a birth-death Monte Carlo Markov chain (MCMC) procedure and reversible jump MCMC, respectively. [*Steinschneider and Lall*, 2015] proposes nonstationary regional frequency analysis conditioned on tropical moisture exports. *O'Connell et al.* [2002] conduct Bayesian flood frequency analysis which incorporates paleohydrologic data and *Renard* [2011] proposes a fully Bayesian approach to regional frequency analysis.

Despite a large body of literature surrounding the topics of multivariate and nonstationary frequency analysis, a comprehensive framework for conducting this analysis has yet to be proposed, which motivates this study. Here we develop a such a framework using a Bayesian hierarchical approach. Section 2 describes the framework in general. The application set up for Taylor Park reservoir, Colorado, USA is then described followed by the specific form of the model and fitting method. Section 5 describes the results, conclusions and discussion of results are presented in section 6.

4.2   Proposed Framework

The proposed framework has three broad components – (i) the model structure composed of an elliptical copula to model the joint dependency and nonstationary marginal GEV models, (ii) computation of the likelihood function and priors and, (iii) estimation of nonstationary return levels.

4.2.1   General model structure

In general we wish to conduct a joint frequency analysis of n variables, $v_1, ..., v_n$ observed over m years. For the model to apply each variable must be an annual or seasonal maxima time-series such that each variable follows a GEV distribution. The general model structure for n variables is

$$(v_1(t), \ldots, v_n(t)) \sim C_g(\Sigma; \{\boldsymbol{\mu}(t), \boldsymbol{\sigma}(t), \boldsymbol{\xi}(t)\}) \tag{4.1}$$

$$v_i(t) \sim GEV(\mu_i(t), \sigma_i(t), \xi_i(t)), \qquad i = 1 \ldots n \tag{4.2}$$

$$\mu_i(t) = g_{\mu i}(\mathbf{x}_i(t)^T, \boldsymbol{\mu}(t), \boldsymbol{\sigma}(t), \boldsymbol{\xi}(t)), \qquad i = 1 \ldots n \tag{4.3}$$

$$\sigma_i(t) = g_{\sigma i}(\mathbf{x}_i(t)^T, \boldsymbol{\mu}(t), \boldsymbol{\sigma}(t), \boldsymbol{\xi}(t)), \qquad i = 1 \ldots n \tag{4.4}$$

$$\xi_i(t) = g_{\xi i}(\mathbf{x}_i(t)^T, \boldsymbol{\mu}(t), \boldsymbol{\sigma}(t), \boldsymbol{\xi}(t)), \qquad i = 1 \ldots n \tag{4.5}$$

where C_g is an n-dimensional Gaussian elliptical copula with dependence matrix Σ, $\mu_i(t), \sigma_i(t)$ and $\xi_i(t)$ are the GEV parameters (location, scale and shape) for variable i at time t, $\boldsymbol{\mu}(t) = [\mu_i(t)]_{i=1}^n$, $\boldsymbol{\sigma}(t) = [\sigma_i(t)]_{i=1}^n$, $\boldsymbol{\xi}(t) = [\xi_i(t)]_{i=1}^n$. The functions $g_{\mu i}(\cdot)$, $g_{\sigma i}(\cdot)$ and $g_{\xi i}(\cdot)$ are (potentially nonlinear) functions of covariates $\mathbf{x}_i(t)^T$ and parameters of other variables. These functions can be used to represent nonlinear dependence relationships between variables. In most cases the $g_{\cdot}(\cdot)$ functions will be linear functions of covariates unless some specific nonlinear dependence structure is required.

The copula dependence matrix, Σ, is a symmetric positive definite matrix capturing the strength of dependence between each pairwise variable. The i,jth element of Σ measures the dependence between variables i and j and can take values between -1 and 1. By definition the dependence between a variable and itself is unity so the diagonal elements of Σ are 1's

$$\Sigma = \begin{bmatrix} 1 & v_{12} & \cdots & v_{1,n-1} & v_{1n} \\ v_{12} & 1 & \ddots & & v_{2n} \\ v_{13} & v_{23} & \ddots & & \vdots \\ \vdots & \vdots & \ddots & 1 & v_{n-1,n} \\ v_{1n} & v_{2n} & \cdots & v_{n-1,n} & 1 \end{bmatrix} \tag{4.6}$$

Note that since Σ is symmetric, there are $n(n-1)/2$ dependence parameters to fit (values in the lower or upper triangle of Σ). For a model with n variables and p covariates for each variable, this framework requires $n(p+3) + n(n-1)/2$ parameters to be estimated.

4.2.2 Gaussian elliptical copula

A Gaussian elliptical copula is a specification for a multivariate distribution with predefined marginals [*Renard and Lang*, 2007]. Because of their ability to represent any marginal distribution, elliptical copulas have become a popular practical tool for modeling multivariate extremes [*Renard*, 2011; *Sang and Gelfand*, 2010; *Ghosh and Mallick*, 2011; *Renard and Lang*, 2007].

Let $\mathbf{V}(t) = (V_1(t), \ldots, V_n(t))$ be a random vector of hydrologic variables at time t and let $\mathbf{v}(t) = (v_1(t), \ldots, v_n(t))$ be a vector of the corresponding realizations. The Gaussian copula constructs the joint cumulative distribution function (cdf) of $\mathbf{V}(t)$ as

$$F_C(\mathbf{v}(t)) = \Phi_\Sigma(\mathbf{u}(t)) \tag{4.7}$$

where $\Phi_\Sigma(\cdot)$ is the joint cdf of an n-dimensional multivariate normal distribution with covariance matrix Σ, $\mathbf{u}(t) = (u_1(t), \ldots, u_n(t))$, $u_i(t) = \phi^{-1}(F_{it}[v_i(t)])$, ϕ^{-1} is the inverse cdf (quantile function) of the standard normal distribution and $F_{it}(\cdot)$ is the marginal GEV cdf of variable i at time t. The corresponding joint pdf is

$$f_C(\mathbf{v}(t)) = \frac{\displaystyle\prod_{i=1}^{n} f_i[v_i(t)]}{\displaystyle\prod_{i=1}^{n} \psi[u_i(t)]} \Psi_\Sigma(\mathbf{u}(t)) \tag{4.8}$$

where $f_{it}(\cdot)$ is the marginal GEV pdf for variable i at time t, $\psi(\cdot)$ is the standard normal pdf and $\Psi_\Sigma(\cdot)$ is the joint pdf of an n-dimensional multivariate normal distribution.

4.2.3 Likelihood and priors

Let $\mathbf{y} = [\mathbf{y}_1, \ldots, \mathbf{y}_n]$ be a matrix of observations where $\mathbf{y}_i = [y_i(t)]_{t=1}^{T}$ is a vector of observations at one site and $\mathbf{y}(t) = [y_i(t)]_{i=1}^{n}$ be a vector of all variables at time t. Let $\mathbf{x}_i = [x_i(t)]_{t=1}^{T}$ be a matrix of covariates for variable i, $X = [\mathbf{x}_1, \ldots, \mathbf{x}_n]$ be a matrix of all covariates and let $\boldsymbol{\theta}$ be a

vector of latent variable parameters for the $g.(\cdot)$ functions. By Bayes' rule the posterior is

$$p(\Sigma, \boldsymbol{\theta}|\mathbf{y}, \mathbf{X}) \propto p(\mathbf{y}, \mathbf{X}|\boldsymbol{\theta})p(\Sigma, \boldsymbol{\theta}) \tag{4.9}$$

where the first term on the right hand side is the copula likelihood which assuming temporal independence can be written

$$p(\Sigma, \boldsymbol{\theta}|\mathbf{y}, \mathbf{X}) = \prod_{t=1}^{m} p(\mathbf{y}(t), \mathbf{X}|\Sigma, \boldsymbol{\theta}) \tag{4.10}$$

where $p(\Sigma, \boldsymbol{\theta}|\mathbf{y}, \mathbf{X})$ is given by the likelihood in equation 4.8.

The marginal GEV likelihood is

$$f_i(y_i(t)|\mu_i(t), \sigma_i, \xi_i) = \frac{1}{\sigma_i} b_i^{-1/\xi_i - 1} \exp\left(-b_i^{-1/\xi_i}\right) \tag{4.11}$$

where

$$b_i = 1 + \xi_i \left(\frac{y_i(t) - \mu_i(t)}{\sigma_i}\right).$$

In practice the logarithm of the posterior is computed to prevent numerical underflow. In this case, the log-likelihood is

$$\log p(\Sigma, \boldsymbol{\theta}|\mathbf{y}, \mathbf{X}) = \log \prod_{i=1}^{n} p(\mathbf{y}(t), \mathbf{x}|\Sigma, \boldsymbol{\beta}, \sigma, \xi) \tag{4.12}$$

$$= \sum_{i=1}^{n} \log f_i[y_i] - \sum_{i=1}^{n} \log \psi[u_i] + \log \Psi_\Sigma(u_1, \ldots, u_n) \tag{4.13}$$

where

$$\sum_{i=1}^{n} \log f_i = -\sum_{i=1}^{n} \left[\log(\sigma_i) + (1 + 1/\xi_i)\log(b_i) + b_i^{-1/\xi_i}\right] \tag{4.14}$$

The term $p(\Sigma, \boldsymbol{\beta}_\mu, \sigma, \xi)$ from equation 4.9 contains prior information. Uninformative priors can be used for most parameters, except for the GEV shape parameters. Informative priors may

be necessary to restrict GEV shape parameters to reasonable ranges for particular variables. For example for precipitation, the shape parameter is usually less the 0.5 and positive so we could apply $p(\xi) \sim N(0, 0.3)$ [*Renard*, 2011] or the so called "geophysical prior" (a shifted beta distribution) [*Martins and Stedinger*, 2010]. Priors such as these can help with model convergence and identifiability [*Renard and Lang*, 2007; *AghaKouchak et al.*, 2013].

4.2.4 Nonstationary return levels

Read and Vogel [2015] suggest it is important to be clear when discussing nonstationary return levels and return periods as there are several definitions [*AghaKouchak et al.*, 2013; *Salas and Obeysekera*, 2014; *Cheng et al.*, 2014]. The return level for a stationary GEV distribution is defined as the $p = (1 - 1/T)$th quantile

$$q_p = \mu + \frac{\sigma}{\xi}[(-\log p)^{-\xi} - 1] \tag{4.15}$$

In a nonstationary setting when the GEV parameters may be time varying, the return level can be computed in each year, which is known as the effective return level [*Cheng et al.*, 2014]

$$q_p(t) = \mu(t) + \frac{\sigma(t)}{\xi(t)}[(-\log p)^{-\xi(t)} - 1] \tag{4.16}$$

In the case of nonstationary GEV parameters, a stationary return level can be computed based on quantiles of the nonstationary parameters

$$\widetilde{q_p} = \widetilde{\mu} + \frac{\widetilde{\sigma}}{\widetilde{\xi}}[(-\log p)^{-\widetilde{\xi}} - 1] \tag{4.17}$$

where

$$\widetilde{\mu} = Q_k(\mu(t_1), \ldots, \mu(t_m)) \tag{4.18}$$

$$\widetilde{\sigma} = Q_k(\sigma(t_1), \ldots, \sigma(t_m)) \tag{4.19}$$

$$\widetilde{\xi} = Q_k(\xi(t_1), \ldots, \xi(t_m)) \tag{4.20}$$

where Q_k indicates computing the kth quantile of the arguments which can be chosen based on the application. For example, choosing $k = 0.5$ would represent the median behavior of each nonstationary GEV parameter.

4.3   Application

During the late 1990s, the Bureau of Reclamation, which maintains over 300 dams located across 17 western states [*Bureau of Reclamation*, 2015], began transitioning to a risk-based approach to assess the safety of dams and prioritize expenditures. Dam safety evaluations and risk analyses require detailed information on extreme flood durations and magnitudes, along with associated probability estimates [*Bureau of Reclamation*, 2003]. Typically, extreme flood frequencies are estimated using statistical and/or rainfall-runoff modeling techniques. For example, in some studies, a frequency curve is fit to peak streamflow observations using maximum likelihood [*OConnell*, 1999] or moments [*Cohn et al.*, 1997; *England*, 1999] and extrapolated to very low probability events (e.g. annual exceedance probabilities less than 0.005). Studies utilizing rainfall-runoff models often involve running thousands to hundreds of thousands of simulations where a precipitation depth (applied to the watershed) is sampled from a site-specific precipitation frequency relationship [*Schaefer et al.*, 2002]. The runoff response for each simulation is recorded as an annual event and later used to generate a statistical flood-frequency relationship using a plotting position technique. Uncertainty analyses are often part of the risk process, though methods used to estimate them vary by study and approach [*Bureau of Reclamation*, 2009, 2013].

In the Intermountain West, melting snowpack is the primary source of spring flood events at many high-elevation watersheds [*Hamlet and Lettenmaier*, 2007]. However, frequency statistics

of snowdepth are not always utilized in dam safety flood frequency analyses, even in watersheds where annual maximum streamflow events are controlled by snowmelt. In this study, we demonstrate an application of the general multivariate, nonstationary frequency analysis presented in the previos section using annual maximum snow water equivalent (SWE), reservoir inflow, and water surface elevation (WSE) for the Taylor Park watershed and Tayloe Park Dam, Colorado, USA (Figure 4.1).
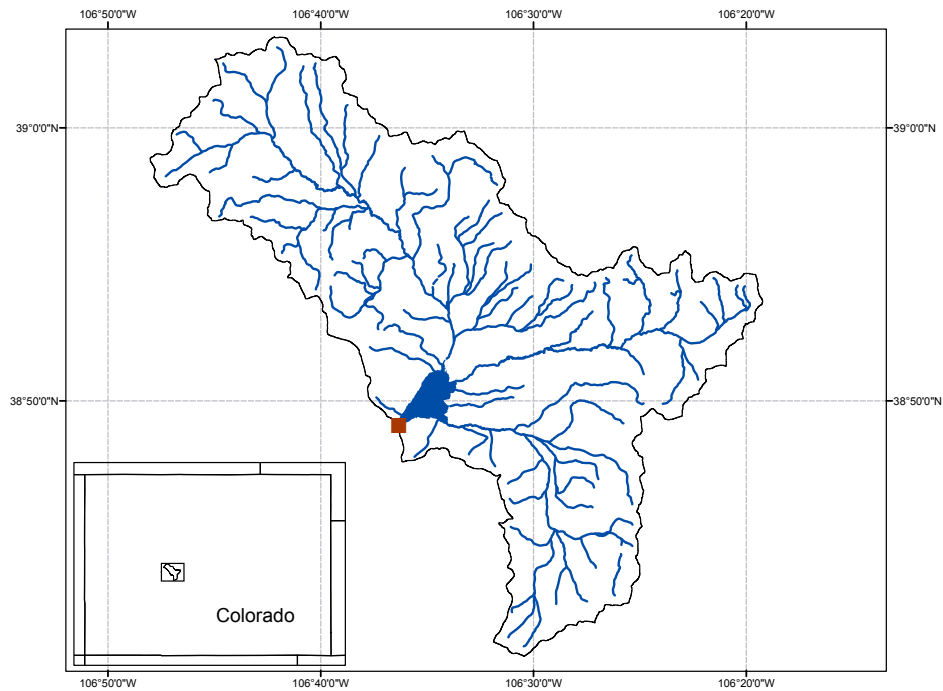
Figure 4.1: Outline of the Taylor Park watershed (255 mi^2; black line) located in Colorado, USA, with National Hydrologic Database stream locations (blue lines). Taylor Park dam is indicated by the brown square.

4.3.1   Data

Daily SWE observations were obtained from sites in the Global Historical Climatology Network *Menne et al.* [2012] that are located within 200 miles of the Taylor Park dam. Daily water surface elevation and naturalized inflow data at the Taylor Park reservoir were downloaded from the Bureau of Reclamation's Upper Colorado Region webpage at `http://www.usbr.gov/rsvrWater/`

`faces/rvrOSMP.xhtml`. We required SWE stations have a minimum of 85% data coverage during the cool-season (October through July) for a minimum of nine years. In addition, for a SWE station to be included, the annual maximum SWE time series had to be significantly correlated with the annual maximum time series of inflow to Taylor Park reservoir. A regional average of peak SWE was used as an indicator of regional snow availability.

Our analysis is restricted to water years from 1981 to 2015 based on the availability of snow data. Annual maximum daily SWE, water surface elevation, and calculated inflow were computed for each water year.
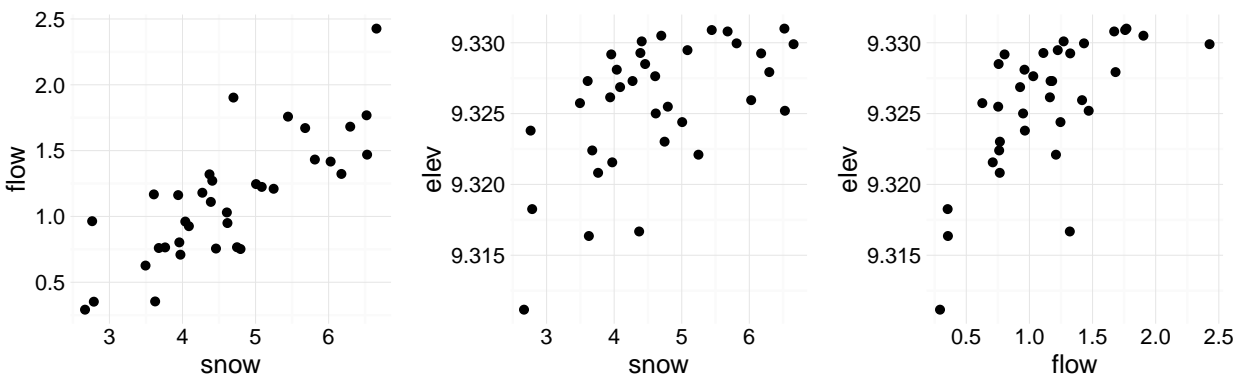
Figure 4.2: Pairwise scatterplots showing the dependence between peak SWE, peak flow and peak elevation for Taylor Park Dam.

4.3.2 Model structure for Taylor Park watershed

In this section we give the structure of the model for the Taylor Park application, which is a special case of the model presented in Section 4.2.1 wherein we can explicitly represent nonlinear dependence between variables.

Let $y(t)$ represent peak SWE, $z(t)$ represent peak flow and $h(t)$ represent peak reservoir elevation. The model structure for these three variables is

$$(y(t), z(t), h(t)) \sim C_g(\Sigma; \{\mu_y(t), \sigma_y, \xi_y, \mu_z(t), \sigma_z, \xi_z, \mu_h(t), \sigma_h, \xi_h\}) \tag{4.21}$$

$$y(t) \sim GEV(\mu_y(t), \sigma_y, \xi_y) \tag{4.22}$$

$$z(t) \sim GEV(\mu_z(t), \sigma_z, \xi_z) \tag{4.23}$$

$$h(t) \sim GEV(\mu_h(t), \sigma_h, \xi_h) \tag{4.24}$$

$$\mu_y(t) = \mu_{y0} + \mathbf{x}_y(t)^T \boldsymbol{\beta}_y \tag{4.25}$$

$$\mu_z(t) = \mu_{z0} + \mathbf{x}_z(t)^T \boldsymbol{\beta}_z \tag{4.26}$$

$$\mu_h(t) = a - \exp(-b\mu_y(t)) \tag{4.27}$$

where $\mathbf{x}_y(t)^T$ and $\mathbf{x}_z(t)^T$ are vectors of climate covariates for $y(t)$ and $z(t)$ respectively, μ_{y0} and μ_{z0} are variable specific intercept terms and $\boldsymbol{\beta}_y$ and $\boldsymbol{\beta}_z$ are vectors of latent regression coefficients. In Equation 4.27 we introduce a hierarchical nonlinear relationship between flow and reservoir elevation motivated by the nonlinear elevation relationships in Figure 4.2, right and middle panels, with parameters a and b controlling the exact shape of the dependence relationship. Equation 4.27 demonstrates how we capture the nonlinear dependence between variables when it is supported by the data. For simplicity we do not introduce time dependence for the scale and location parameters though this could be incorporated in a similar manner as the location parameter. In terms of the general model notation in Section 4.2.3, $\boldsymbol{\theta} = [\mu_{y0}, \boldsymbol{\beta}_y, \sigma_y, \xi_y, \mu_{z0}, \boldsymbol{\beta}_z, \sigma_z, \xi_z, a, b]$ and $\mathbf{X} = [\mathbf{x}_y(t)^T, \mathbf{x}_z(t)^T]_{t=1}^m$.

The copula dependence matrix is

$$\Sigma = \begin{bmatrix} 1 & \nu_{yz} & \nu_{yh} \\ \nu_{yz} & 1 & \nu_{zh} \\ \nu_{yh} & \nu_{zh} & 1 \end{bmatrix} \tag{4.28}$$

where ν_{ij} represents the dependence (correlation) between variable i and j.

4.3.3   Covariates

We used indicies of the El Niño Southern Oscillation (ENSO), the Pacific Decadal Oscillation (PDO) and the Atlantic Multidecadal Oscillation (AMO) as covariates. We obtained values of the multivariate ENSO index (MEI) [*Wolter and Timlin*, 1998, 1993] from `http://www.esrl.noaa.gov/psd/enso/mei/`. PDO values [*Zhang et al.*, 1997] were obtained from `http://research.jisao.washington.edu/pdo/`. AMO values [*Enfield et al.*, 2001] were obtained from `http://www.esrl.noaa.gov/psd/data/timeseries/AMO/`.

Peak SWE is expected to depend on winter values of each index so we used winter (DJF) average values for covariates (ref?). Peak flow is expected to depend partially on snow (which is captured by the copula) and on spring values of each climate index, so we used spring (MAM) average values as covariates. The covariates vectors at time t are

$$\mathbf{x}_y(t)^T = [1, t, \text{MEI}_w(t), \text{PDO}_w(t), \text{AMO}_w(t)] \tag{4.29}$$

$$\mathbf{x}_z(t)^T = [1, t, \text{MEI}_s(t), \text{PDO}_s(t), \text{AMO}_s(t)] \tag{4.30}$$

where a w subscript denotes a winter average index and an s subscript denotes a spring average index.

4.3.4   Adequacy of the Gaussian Copula

The Gaussian copula is a flexible tool for modeling multivariate distributions with prescribed marginal distributions [*Renard and Lang*, 2007]. Despite its flexibility, the Gaussian copula may not be appropriate for a given dataset, that is the data may not be multivariate normally distributed after transformation using $\phi^{-1}(F_i(y_i))$ where ϕ^{-1} is the inverse cumulative standard normal distribution function and F_i is the GEV distribution function for variable y_i. To test multivariate normality of the the data we ran three tests, (1) Henze-Zirkler's [*Henze and Zirkler*, 1990], (2) Mardia's [*Mardia*, 1970] and (3) Royston's [*Royston*, 1982] multivariate normality test using

marginal transformations based on the MLE GEV fits, all of which indicated the transformed data follow a multivariate normal distribution.

The Gaussian copula should be considered a practical tool for modeling multivariate extremes as it is not based on any theoretical arguments. However, its lack of asymptotic dependence may lead to underestimation of low probability events when used to extrapolate with data that exhibits tail dependence [*Renard and Lang*, 2007]. *Renard and Lang* [2007] suggest that the Gaussian copula is most useful in the observations range. In the results section we show quantile curves extrapolated beyond the range of the data for the purposes of comparing uncertainty estimates.

4.3.5 Model fitting

The model was fit using a Monte Carlo Markov Chain (MCMC) procedure, specifically, a univariate slice sampler [*Neal*, 2003] within a Gibbs sampler. In this scheme, slice sampling is applied to sample from the conditional distribution of each parameter given all other parameters. We ran three chains of length 100,000, discarding the first 50,000 iterations as burn-in and retaining only every ten samples afterwards, resulting in 15,000 posterior samples. To assess convergence, the $\hat{R}$ statistic [*Gelman and Rubin*, 1992] was computed for each parameter, ensuring that the value was less than 1.1.

4.3.6 Model comparison

We compare four related models to highlight the advantages of conducting a multivariate frequency analysis. The four models are

(1) **Stationary Independent GEV model fit with MLE**. A univariate stationary GEV distribution is fit independently to each variable using MLE.

(2) **Nonstationary Independent GEV model fit with MLE**. A univariate nonstationary GEV distribution is fit to each variable using MLE where the mean is allowed to vary over time according to linear trend and climate covariates.

(3) **Nonstationary Independent GEV model fit with MCMC**. A univariate nonstationary GEV distribution is fit to each variable using MCMC where the mean is allowed to vary over time according to linear trend and climate covariates.

(4) **Nonstationary Joint GEV model fit with MCMC**. A multivariate Gaussian elliptical copula with nonstationary GEV marginals is fit to all variables simultaneously.

Uncertainty in the MLE models was estimated by simulating draws from a multivariate normal distribution using the observed covariance matrix of the parameters (computed from the Hessian matrix evaluated at the posterior mode produced by the optimizer).

4.4   Results

Figure 4.3 shows the nonstationary return levels for the 100-year return period from the Bayesian independent model (left column), the Bayesian joint model (middle column) and the MLE independent model for the three variables – reservoir elevation (top row), peak flow (middle row) and peak SWE (bottom row). The whiskers show the 90% credible intervals, the boxes the interquartile range and the horizontal lines inside the boxes, the median. The reduction in uncertainty in the joint model compared to the independent models is apparent in all variables. Although all models use the same climate covariates, the MLE independent model is less sensitive to the climate covariates. Both Bayesian models show similar trends but with increased uncertainty in the independent case. A downward linear trend is apparent in all variables and models. The top of the dam is 9.343 kilo-feet and the MLE independent model consistently estimates higher reservoir water levels for the 100-year return (top right panel), which seems unrealistic, compared to the other two models. This is consistent with the model's insensitivity to climate covariates.

To compare the uncertainty estimates of all models, stationary return levels were computed from the nonstationary models using Equation 4.17. That is, the 50th percentile of the nonstationary location parameter estimates were computed ($k = 0.50$) and used to compute stationary return levels for a range of return periods (1–1000 year). Figure 4.4 shows the width of the 90% credi-
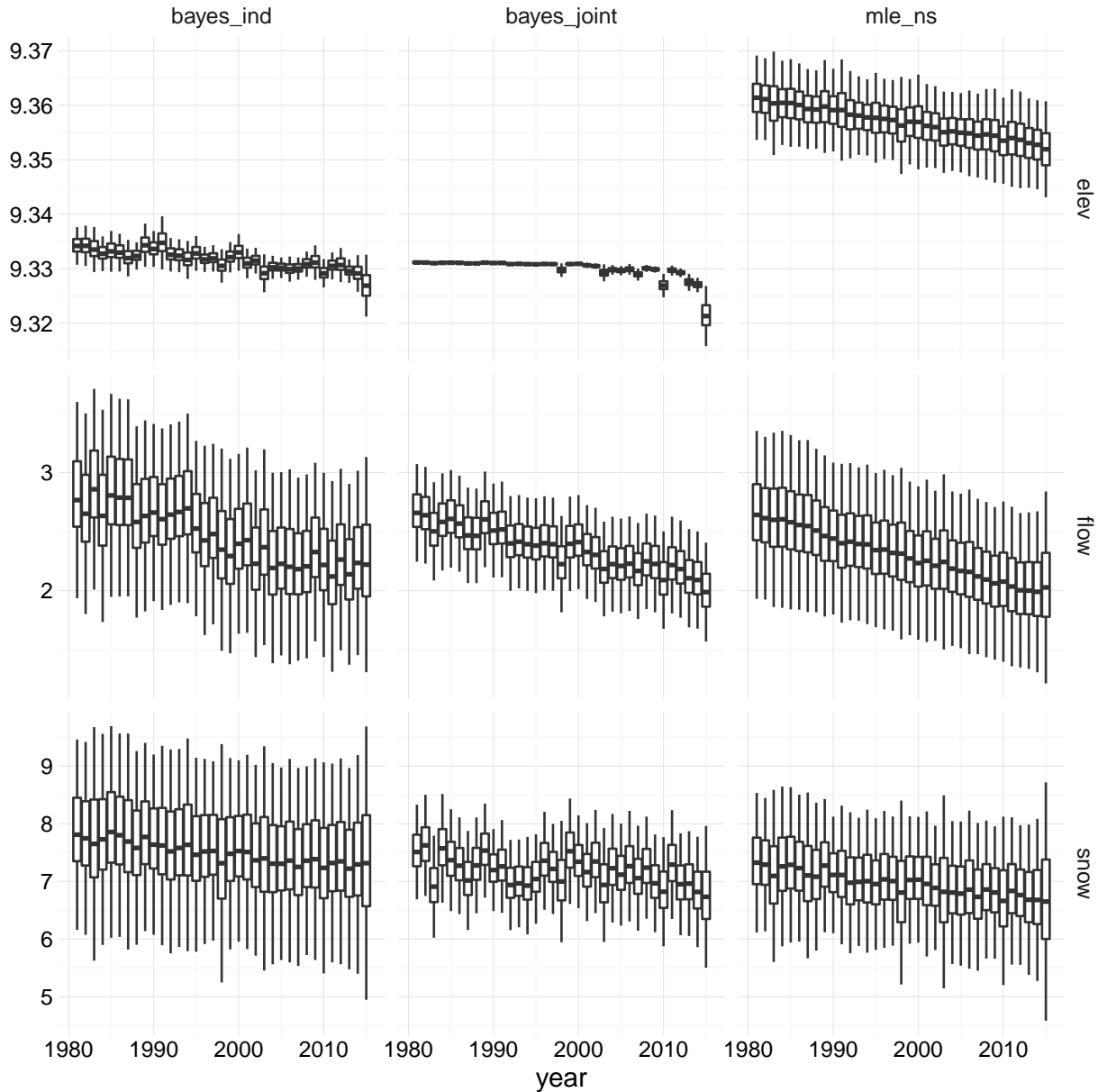
Figure 4.3: Nonstationary 100 year return levels from the independent Bayesian model (left column), the joint Bayesian model (middle column), and from the independent MLE model (right column). Reservoir elevation is shown in the top row, peak flow in the middle row and peak SWE in the bottom row.

ble intervals for return levels plotted for a range of return periods. Smaller values of the width indicate lower uncertainty. The Bayesian joint model consistently produces lower uncertainty intervals than either the Bayesian independent model or the MLE independent model.
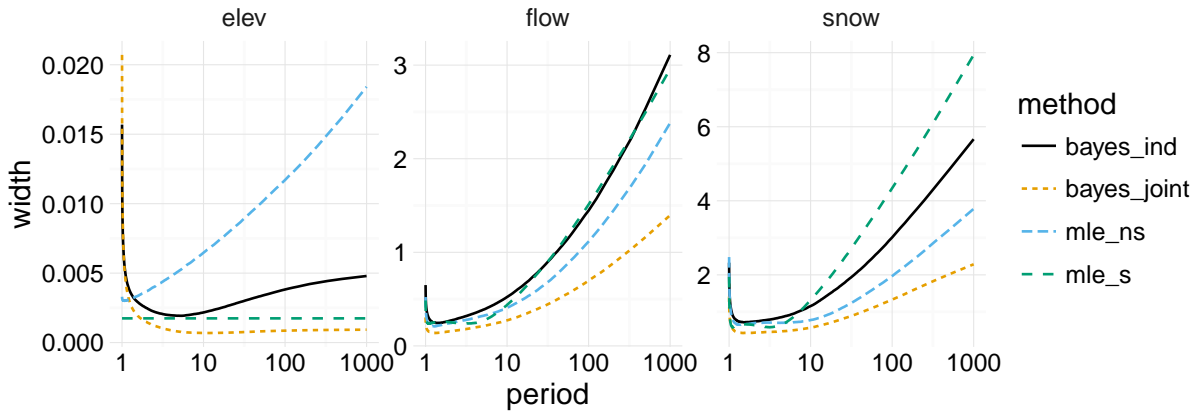
Figure 4.4: Width of the 90% credible intervals of return periods highlighting the reduction of uncertainty by conducting a joint frequency analysis.

The simulated model dependence structure between the variables using the Guassian copula and without, are compared with the observations (Figure 4.5, bottom). It can be seen that the copula captures the structure of the pairwise dependence better (Figure 4.5, bottom) as compared to the simulations without the copula (Figure 4.5, top). This property is important for simulating extremes while maintaining multivariate dependence.
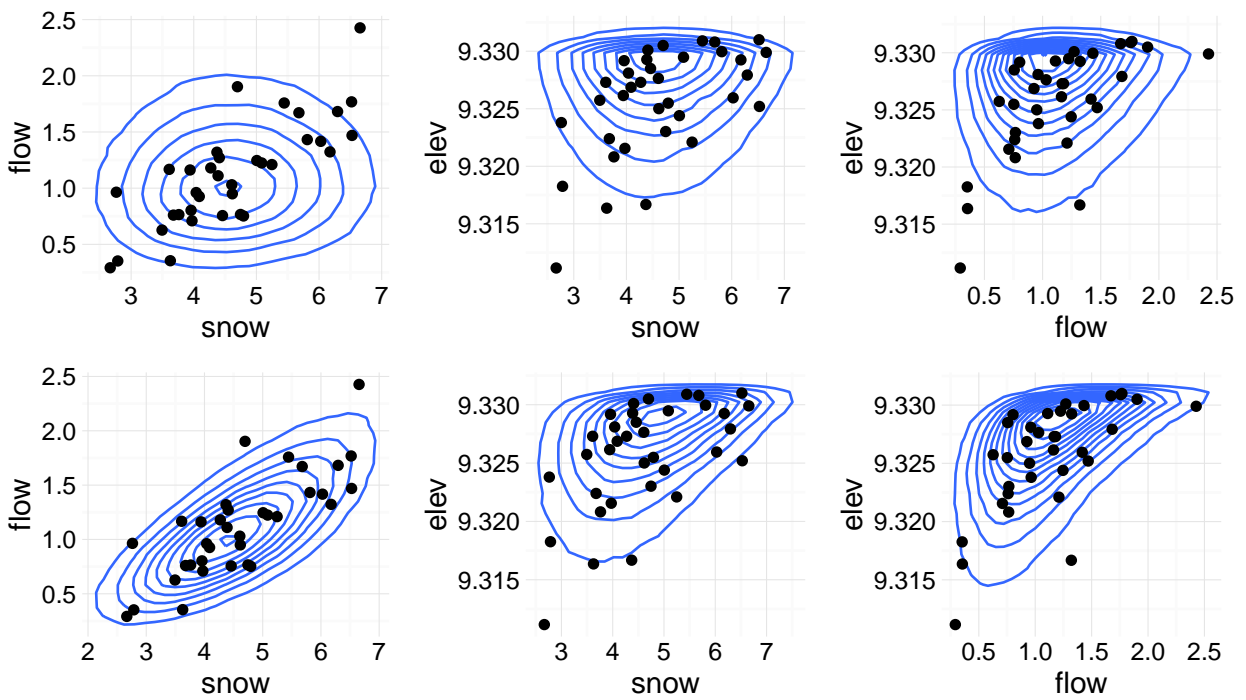
Figure 4.5: Pairwise dependence structure simulated without the copula (top row) and with the copula (bottom row). Observations are shown as black points.

4.5   Conclusion and Discussion

In this study, we presented a Bayesian hierarchical framework for modeling multivariate nonstationary frequency for hydrologic variables. The general framework assumes the marginal distribution of each variable is GEV where the distribution parameters can vary in time as a function of covariates and of other model parameters. Multivariate dependence between variables is captured using a Gaussian elliptical copula.

We applied this framework to conduct a joint frequency analysis of peak SWE, peak inflow and peak reservoir elevation for Taylor Park Reservoir, Colorado, USA. This application incorporated large scale climate covariates and a nonlinear relationship between flow and reservoir elevation. We found that the Bayesian approach provided robust estimation of uncertainties of the return levels and furthermore, use of the copula decreased uncertainty in return level estimates and captured the multivariate dependence between these three variables with high fidelity to the observed data.

The proposed Bayesian multivariate nonstationary framework has several benefits when compared to stationary, independent and non-Bayesian versions:

- **Reduction of uncertainty** - By incorporating multivariate dependence between variables, overall uncertainty was reduced.

- **Variable dependence** - Linear dependence relationships between variables can be captured by using the copula.

- **Climate covariates** - Covariates representing large scale climate influences can be included to capture decadal and multidecadal climate oscillations.

- **Hierarchical dependence** - Nonlinear dependence between variables (such as with flow and reservoir elevation) can be captured by incorporating nonlinear relationships between model parameters.

The Gaussian copula is a flexible tool for modeling multivariate dependence between variables but may not always be appropriate in every application. For example, *Renard and Lang* [2007] give an example using peak flow and peak volume data from the Ubaye river at Barcelonette, France – wherein, peak flows are generated by either snow melt or heavy rainfall and capturing this relationship with a single dependence parameter leads to poor results. It is therefore important to test for multivariate normality of a dataset before a multivariate frequency analysis is conducted. The Gaussian copula also assumes asymptotic independence; in applications where tail dependence is present, extrapolating using the Gaussian copula may lead to underestimation of risk.

In the application we have presented, the scale and shape parameters were assumed to be stationary for simplicity. However, this assumption can be easily relaxed by adding covariates for these GEV parameters as well. While the proposed framework is focused on nonstationary analysis of three variables, with minimal effort this framework can be modified to include a spatial component to model multivariate extremes at several locations – such as on a river network, something we plan to investigate further.

4.6   Acknowledgments

Pre- and postprocessing analysis was conducted using the R language [*R Core Team*, 2014].

Chapter 5

Conclusions and future work

This dissertation presented four chapters related to characterizing and modeling hydroclimate extremes in the western US, falling under the broad categories of seasonal, spatial, nonstationary and multivariate extremes.

In Chapter 1, we presented a detailed analysis of 3-day total extreme precipitation throughout the western United States. Using an improved extreme value clustering method, we defined spatially coherent regions for extremes that vary seasonally and made physical sense based on topography. Based on storm back trajectory analysis, we were able to demonstrate unique moisture sources and dominant moisture pathways for each spatial region. This analysis opens the door to many new applications. By sampling the trajectory data conditioned on features such as current location of trajectories, sea surface temperatures, etc., short term projections of spatially coherent extremes can be made. This resampling is akin to generating hurricane tracks [*Yonekura and Hall*, 2011, for example]. The trajectory projections can be coupled with spatial extremes model [*Cooley et al.*, 2007, for example] to produce return level maps of extreme precipitation, and consequently hydrologic extremes, important for resource management. Furthermore, these trajectories can be resampled to produce physically based simulations of extreme precipitation. We can also investigate the climatic conditions in moisture source regions that favor the production of extremes, potentially to develop statistical forecast models. Finally, given the evidence of the land surface as a moisture source for some regions, we would like to investigate the relative contribution of the land surface versus open water bodies as a moisture source for extreme precipitation.

In Chapter 2, we describe a general Bayesian hierarchical model for extreme data observed over space and time. The data is assumed to originate from a Gaussian elliptical copula having generalized extreme value (GEV) marginal distributions. Spatial dependence is further captured by Gaussian processes on the three GEV parameters (location, scale and shape). Using a composite likelihood approach, we are able to incorporate 2595 observation locations with 54 years of data. With spatially varying regression coefficients, the model can be applied to arbitrarily large regions. The model was applied to extreme 3-day precipitation in fall in the western United States, a climatologically and geographically diverse region. The model was fit using a standard Bayesian methodology, implicitly capturing uncertainty in the parameter estimates and spatial predictions. A number of extensions can be made to this framework. The most obvious extension is to allow temporal variation in the GEV parameters by including temporal covariates. While this extension remains infeasible for the size of the current study region, it may be feasible for smaller regions, say a single state or moderate sized river basin. Additional spatial covariates could be included; for example, seasonal temperature, winds or evapo-transpiration. A model such as the one presented here can be used to investigate changes in risk under specific climate regimes (i.e. ENSO); one would simply include the mean seasonal precipitation field from strong El Niño or La Niña years. Because we incorporate a data layer, this model could be used to simulate realistic fields of extremes under specific climate regimes. Finally, we plan to explore the linking of streamflow data into the hierarchy, so that streamflow extremes can be simultaneously estimated.

In Chapter 3, we presented a model for joint Bayesian hierarchical nonstationary regional frequency analysis of precipitation and streamflow extremes where nonstationarity was induced by large scale climate covariates. Joint behavior was captured at the data level by a Gaussian elliptical copula and at the parameter level by linearly linking the GEV location parameters. This approach is particularly useful for data limited regions as an alternative to RFA. Any number of precipitation and streamflow stations may be included without the need for delineation of homogeneous regions. Though we demonstrated this approach with a single streamflow site, the model could be easily modified to allow for multiple flow locations. In this same fashion, the model could

be modified to include other atmospheric or hydrologic variables. Spatial covariates and spatial processes on the GEV parameters could also be included to allow for full spatial analysis.

In Chapter 4, we presented a Bayesian hierarchical framework for modeling multivariate nonstationary frequency for hydrologic variables. The general framework assumes the marginal distribution of each variable is GEV where the distribution parameters can vary in time as a function of covariates and of other model parameters. Multivariate dependence between variables is captured using a Gaussian elliptical copula. In the application we have presented, the scale and shape parameters were assumed to be stationary for simplicity. However, this assumption can be easily relaxed by adding covariates for these GEV parameters as well. While the proposed framework is focused on nonstationary analysis of three variables, with minimal effort this framework can be modified to include a spatial component to model multivariate extremes at several locations – such as on a river network, something we plan to investigate further.

Bibliography

AghaKouchak, A., D. Easterling, K. Hsu, S. Schubert, and S. Sorooshian (Eds.), *Extremes in a changing climate: detection, analysis and uncertainty*, Springer, 2013.

Alexander, L. V., et al., Global observed changes in daily climate extremes of temperature and precipitation, *Journal of Geophysical Research: Atmospheres*, *111*(D5), D05,109, 2006.

Alexander, M. A., J. D. Scott, D. Swales, M. Hughes, K. Mahoney, and C. A. Smith, Moisture Pathways into the US Intermountain West Associated with Heavy Winter Precipitation Events, *Journal of Hydrometeorology*, 2015.

Apipattanavis, S., B. Rajagopalan, and U. Lall, Local Polynomial–Based Flood Frequency Estimator for Mixed Population, *Journal of Hydrologic Engineering*, *15*(9), 680–691, 2010.

Apputhurai, P., and A. G. Stephenson, Spatiotemporal hierarchical modelling of extreme precipitation in Western Australia using anisotropic Gaussian random fields, *Environmental and Ecological Statistics*, *20*(4), 667–677, 2013.

Arriaga Ramírez, S., and T. Cavazos, Regional trends of daily precipitation indices in northwest Mexico and southwest United States, *Journal of Geophysical Research: Atmospheres*, *115*(D14), D14,111, 2010.

Aryal, S. K., B. C. Bates, E. P. Campbell, Y. Li, M. J. Palmer, and N. R. Viney, Characterizing and Modeling Temporal and Spatial Trends in Rainfall Extremes, *Journal of Hydrometeorology*, *10*(1), 241–253, 2009.

Aryal, S. K., B. C. Bates, E. P. Campbell, Y. Li, M. J. Palmer, and N. R. Viney, Characterizing and Modeling Temporal and Spatial Trends in Rainfall Extremes, *dx.doi.org*, *10*(1), 241–253, 2010.

Atyeo, J., and D. Walshaw, A region-based hierarchical model for extreme rainfall over the UK, incorporating spatial dependence and temporal trend, *Environmetrics*, *23*(6), 509–521, 2012.

Balling Jr, R. C., and G. B. Goodrich, Spatial analysis of variations in precipitation intensity in the USA, *Theoretical and Applied Climatology*, *104*(3-4), 415–421, 2011.

Banerjee, S., A. E. Gelfand, A. O. Finley, and H. Sang, Gaussian predictive process models for large spatial data sets, *Journal of the Royal Statistical Society*, 2008.

Bernard, E., P. Naveau, M. Vrac, and O. Mestre, Clustering of Maxima: Spatial Dependencies among Heavy Rainfall in France, 2013.

Betancourt, M. J., Generalizing the No-U-Turn Sampler to Riemannian Manifolds, *arXiv*, *1304*(1920), 2013.

Bobée, B., The Log Pearson type 3 distribution and its application in hydrology, *Water Resources Research*, *11*(5), 681–689, 1975.

Bobee, B. B., and R. Robitaille, The use of the Pearson type 3 and log Pearson type 3 distributions revisited, *Water Resources Research*, *13*(2), 427–443, 1977.

Bosilovich, M. G., and S. D. Schubert, Precipitation recycling over the central United States diagnosed from the GEOS-1 data assimilation system, *Journal of Hydrometeorology*, 2001.

Bosilovich, M. G., M. Rixen, P. van Oevelen, G. Asrar, G. Compo, A. Simmons, and K. Trenberth, Report of the 4th World Climate Research Programme International Conference on Reanalyses, *Tech. rep.*, NASA Global Modeling and Assimilation Office, Silver Spring, Maryland, USA, 2012.

Bracken, C., B. Rajagopalan, M. Alexander, and S. Gangopadhyay, Spatial variability of seasonal extreme precipitation in the western United States, *Journal of Geophysical Research: Atmospheres*, *120*(10), 4522–4533, 2015.

Bracken, C., B. Rajagopalan, L. Cheng, W. Kleiber, and S. Gangopadhyay, Spatial Bayesian hierarchical modeling of precipitation extremes over a large domain, *Water Resources Research*, (In Review), 2016.

Bradley, A. A., Regional frequency analysis methods for evaluating changes in hydrologic extremes, *Water Resources Research*, *34*(4), 741–750, 1998.

Bureau of Reclamation, Probabilistic Extreme Flood Hydrographs That Use PaleoFlood Data for Dam Safety Applications, *Tech. rep.*, United States Bureau of Reclamation, 2003.

Bureau of Reclamation, Trinity Dam Detailed Hydrologic Hazard Analysis Using the Stochastic Event Flood Model, *Tech. rep.*, United States Bureau of Reclamation, 2009.

Bureau of Reclamation, Friant Dam Hydrologic Hazard for Issue Evaluation, *Tech. rep.*, United States Bureau of Reclamation, 2013.

Bureau of Reclamation, About Us, available at `http://www.usbr.gov/main/about/fact.html`, 2015.

Caragea, P. C., and R. L. Smith, Approximate Likelihoods for Spatial Processes, in *Joint Statistical Meetings*, pp. 385–390, 2006.

Caragea, P. C., and R. L. Smith, Asymptotic properties of computationally efficient alternative estimators for a class of multivariate normal models, *Journal of Multivariate Analysis*, *98*(7), 1417–1440, 2007.

Cayan, D. R., K. T. Redmond, and L. G. Riddle, ENSO and Hydrologic Extremes in the Western United States, *Journal of Climate*, *12*(9), 2881–2893, 1999.

Cayan, D. R., M. D. Dettinger, H. F. Diaz, and N. E. Graham, Decadal Variability of Precipitation over Western North America, *Journal of Climate*, *11*(12), 3148–3166, 2010.

Chebana, F., and T. B. M. J. Ouarda, Multivariate quantiles in hydrological frequency analysis, *Environmetrics*, *22*(1), 63–78, 2011.

Chebana, F., C. Charron, T. B. M. J. Ouarda, and B. Martel, Regional Frequency Analysis at Ungauged Sites with the Generalized Additive Model, *Journal of Hydrometeorology*, *15*(6), 2418–2428, 2014.

Cheng, L., A. AghaKouchak, E. Gilleland, and R. W. Katz, Non-stationary extreme value analysis in a changing climate, *Climatic Change*, *127*(2), 353–369, 2014.

Cheng, L., B. Rajagopalan, A. AghaKouchak, C. Bracken, and J. Eischeid, A Nonstationary Spatio-temporal Framework for Climate-Informed Extreme Precipitation Analysis, *Water Resources Research*, (In Review), 2016.

Cohn, T., W. Lane, and W. Baier, An algorithm for computing moments-based flood quantile estimates when historical flood information is available, *Water Resources Research*, *33*(9), 2089–2096, 1997.

Coles, S., *An Introduction to Statistical Modeling of Extreme Values*, Springer Series in Statistics, Springer London, London, 2001.

Cooley, D., and S. R. Sain, Spatial Hierarchical Modeling of Precipitation Extremes From a Regional Climate Model, *Journal of Agricultural, Biological, and Environmental Statistics*, *15*(3), 381–402, 2010.

Cooley, D., P. Naveau, and P. Poncet, Variograms for spatial max-stable random fields, *Dependence in probability and statistics*, 2006.

Cooley, D., D. Nychka, and P. Naveau, Bayesian spatial modeling of extreme precipitation return levels, *Journal of the American Statistical Association*, 2007.

Dales, M. Y., and D. W. Reed, Regional flood and storm hazard assessment - NERC Open Research Archive, 1989.

Davison, A. C., S. A. Padoan, and M. Ribatet, Statistical Modeling of Spatial Extremes, *Statistical Science*, *27*(2), 161–186, 2012.

Dee, D. P., et al., The ERA-Interim reanalysis: configuration and performance of the data assimilation system, *Quarterly Journal of the Royal Meteorological Society*, *137*(656), 553–597, 2011.

DeFlorio, M. J., D. W. Pierce, D. R. Cayan, and A. J. Miller, Western U.S. Extreme Precipitation Events and Their Relation to ENSO and PDO in CCSM4, *26*(12), 4231–4243, 2013.

DeGaetano, A. T., A Smirnov test–based clustering algorithm with application to extreme precipitation data, *Water Resources Research*, 1998.

DeGaetano, A. T., Spatial grouping of United States climate stations using a hybrid clustering approach, *International Journal of Climatology*, 2001.

Dirmeyer, P. A., J. Wei, and M. G. Bosilovich, Comparing Evaporative Sources of Terrestrial Precipitation and Their Extremes in MERRA Using Relative Entropy, *Journal of Geophysical Research: Atmospheres*, 2014.

Dorling, S. R., T. D. Davies, and C. E. Pierce, Cluster analysis: A technique for estimating the synoptic meteorological controls on air and precipitation chemistry—Method and applications, *Atmospheric Environment. Part A. General Topics*, *26*(14), 2575–2581, 1992.

Dos Santos, C., C. Neale, and T. Rao, Trends in indices for extremes in daily temperature and precipitation over Utah, USA, *International Journal Climatology*, 2011.

Draxler, R. R., and G. D. Hess, Description of the HYSPLIT4 modeling system, *Techreport*, p. 24pp, 1997.

Draxler, R. R., and G. D. Hess, An overview of the HYSPLIT4 modelling system for trajectories, *Australian Meteorological Magazine*, 1998.

Draxler, R. R., B. Stunder, and G. Rolph, HYSPLIT4 user's guide, *Techreport*, 1999.

Dulière, V., Y. Zhang, and E. P. Salathé Jr., Changes in Twentieth-Century Extreme Temperature and Precipitation over the Western United States Based on Observations and Regional Climate Model Simulations*, *26*(21), 8556–8575, 2013a.

Dulière, V., Y. Zhang, and E. P. Salathé Jr., Changes in Twentieth-Century Extreme Temperature and Precipitation over the Western United States Based on Observations and Regional Climate Model Simulations*, *26*(21), 8556–8575, 2013b.

Durre, I., M. J. Menne, and R. S. Vose, Strategies for Evaluating Quality Assurance Procedures, *Journal of Applied Meteorology and Climatology*, *47*(6), 1785–1791, 2008.

Durre, I., M. J. Menne, B. E. Gleason, T. G. Houston, and R. S. Vose, Comprehensive Automated Quality Assurance of Daily Surface Observations, *Journal of Applied Meteorology and Climatology*, *49*(8), 1615–1633, 2010.

Dyrrdal, A. V., A. Lenkoski, T. L. Thorarinsdottir, and F. Stordal, Bayesian hierarchical modeling of extreme hourly precipitation in Norway, *Environmetrics*, 2014.

El Adlouni, S., and T. B. M. J. Ouarda, Joint Bayesian model selection and parameter estimation of the generalized extreme value model with covariates using birth-death Markov chain Monte Carlo, *Water Resources Research*, *45*(6), 1–11, 2009.

Enfield, D. B., A. M. Mestas Nuñez, and P. J. Trimble, The Atlantic Multidecadal Oscillation and its relation to rainfall and river flows in the continental U.S., *Geophysical Research Letters*, *28*(10), 2077–2080, 2001.

England, J. F., Draft users manual for program ema, at-site flood frequency analysis with historical/paleohydrologic data, *Bureau of Reclamation, Technical Service Center, Denver, Colorado*, 1999.

Favre, A. C., S. El Adlouni, L. Perreault, N. Thiémonge, and B. Bobée, Multivariate hydrological frequency analysis using copulas, *Water Resources Research*, *40*(1), 1–12, 2004.

Feldl, N., and G. H. Roe, Climate Variability and the Shape of Daily Precipitation: A Case Study of ENSO and the American West, *dx.doi.org*, *24*(10), 2483–2499, 2011.

Fuentes, M., Approximate Likelihood for Large Irregularly Spaced Spatial Data, *Journal of the American Statistical Association*, *102*(477), 321–331, 2007.

Gelman, A., and D. B. Rubin, Inference from Iterative Simulation Using Multiple Sequences, *Statistical Science*, *7*(4), 457–472, 1992.

Genolini, C., and B. Falissard, KmL: k-means for longitudinal data, *Computational Statistics*, *25*(2), 317–328, 2010.

Genolini, C., and B. Falissard, Kml: A package to cluster longitudinal data, *Computer Methods and Programs in Biomedicine*, *104*(3), e112–e121, 2011.

Gershunov, A., and T. P. Barnett, ENSO Influence on Intraseasonal Extreme Rainfall and Temperature Frequencies in the Contiguous United States: Observations and Model Results, *11*(7), 1575–1586, 1998.

Ghosh, S., and B. K. Mallick, A hierarchical Bayesian spatio-temporal model for extreme precipitation events, *Environmetrics*, *22*(2), 192–204, 2011.

Groisman, P. Y., R. W. Knight, and T. R. Karl, Heavy Precipitation and High Streamflow in the Contiguous United States: Trends in the Twentieth Century, *Bull. Amer. Meteor. Soc.*, *82*(2), 219–246, 2001.

Gumbel, E. J., The Return Period of Flood Flows, *The annals of mathematical statistics*, 1941.

Gustafsson, M., D. Rayner, and D. Chen, Extreme rainfall events in southern Sweden: where does the moisture come from?, *Tellus A*, *62*(5), 605–616, 2010.

Hamlet, A. F., and D. P. Lettenmaier, Effects of 20th century warming and climate variability on flood risk in the western us, *Water Resources Research*, *43*(6), 2007.

Heagerty, P. J., and S. R. Lele, A Composite Likelihood Approach to Binary Spatial Data, *Journal of the American Statistical Association*, *93*(443), 1099, 1998.

Henze, N., and B. Zirkler, A class of invariant consistent tests for multivariate normality, *Communications in Statistics - Theory and Methods*, *19*(10), 3595–3617, 1990.

Higgins, R. W., J.-K. E. Schemm, W. Shi, and A. Leetmaa, Extreme Precipitation Events in the Western United States Related to Tropical Forcing, *Journal of Climate*, *13*(4), 793–820, 2010.

Hoffman, M. D., and A. Gelman, The No-U-Turn Sampler: Adaptively Setting Path Lengths in Hamiltonian Monte Carlo, *Journal of Machine Learning Research*, *15*(Apr), 1593–1623, 2014.

Hosking, J. R. M., and J. R. Wallis, Some statistics useful in regional frequency analysis, *Water Resources Research*, *29*(2), 271–281, 1993.

Hosking, J. R. M., J. R. WALLIS, and E. F. WOOD, An appraisal of the regional flood frequency procedure in the UK Flood Studies Report, *Hydrological Sciences Journal*, *30*(1), 85–109, 1985.

Hsu, K. C., and S. T. Li, Clustering spatial–temporal precipitation data using wavelet transform and self-organizing map neural network, 2010.

Izquierdo, R., A. Avila, and M. Alarcón, Trajectory statistical analysis of atmospheric transport patterns and trends in precipitation chemistry of a rural site in NE Spain in 1984–2009, *Atmospheric Environment*, *61*, 400–408, 2012.

Janssen, E., D. J. Wuebbles, K. E. Kunkel, S. C. Olsen, and A. Goodman, Observational- and model-based trends and projections of extreme precipitation over the contiguous United States, *Earth's Future*, *2*(2), 99–113, 2014.

Jiang, T., K. J. Evans, Y. Deng, and X. Dong, Intermediate frequency atmospheric disturbances: A dynamical bridge connecting western U.S. extreme precipitation with East Asian cold surges, *Journal of Geophysical Research: Atmospheres*, *119*(7), 3723–3735, 2014.

Johnson, M. E., L. M. Moore, and D. Ylvisaker, Minimax and maximin distance designs, *Journal of Statistical Planning and Inference*, *26*(2), 131–148, 1990.

Jones, M. R., S. Blenkinsop, and H. J. Fowler, Objective classification of extreme rainfall regions for the UK and updated estimates of trends in regional extreme rainfall, *International Journal of Climatology*, 2014.

Jorba, O., C. Pérez, F. Rocadenbosch, and J. M. Baldasano, Cluster Analysis of 4-Day Back Trajectories Arriving in the Barcelona Area, Spain, from 1997 to 2002, *Journal of Applied Meteorology*, *43*(6), 887–901, 2004.

Kalnay, E., et al., The NCEP/NCAR 40-Year Reanalysis Project, *Bull. Amer. Meteor. Soc.*, *77*(3), 437–471, 2011.

Kao, S.-C., and R. S. Govindaraju, A bivariate frequency analysis of extreme rainfall with implications for design, *Journal of Geophysical Research: Atmospheres*, *112*(D13), 1–15, 2007.

Katz, R. W., Statistics of extremes in climate change, *Climatic Change*, *100*(1), 71–76, 2010.

Katz, R. W., M. B. Parlange, and P. Naveau, Statistics of extremes in hydrology, *Advances in Water Resources*, *25*(8-12), 1287–1304, 2002.

Kaufman, L., and P. Rousseeuw, *Finding Groups in Data: An Introduction to Cluster Analysis*, Wiley, 1990.

Kunkel, K. E., Sea surface temperature forcing of the upward trend in U.S. extreme precipitation, *Journal of Geophysical Research: Atmospheres*, *108*(D1), ACL 6–1–ACL 6–10, 2003a.

Kunkel, K. E., North American Trends in Extreme Precipitation, *Natural Hazards*, *29*(2), 291–305, 2003b.

Kunkel, K. E., K. Andsager, and D. R. Easterling, Long-Term Trends in Extreme Precipitation Events over the Conterminous United States and Canada, *Journal of Climate*, *12*(8), 2515–2527, 1999.

Kunkel, K. E., D. R. Easterling, K. Redmond, and K. Hubbard, Temporal variations of extreme precipitation events in the United States: 1895–2000, *Geophysical Research Letters*, *30*(17), 1900, 2003.

Lima, C. H. R., U. Lall, T. J. Troy, and N. Devineni, A climate informed model for nonstationary flood risk prediction: Application to Negro River at Manaus, Amazonia, *Journal of Hydrology*, *522*, 594–602, 2015.

Lindsay, B. G., Composite Likelihood Methods, *Comtemporary Mathematics*, *80*, 221–239, 1988.

Lu, M., U. Lall, A. Schwartz, and H. Kwon, Precipitation predictability associated with tropical moisture exports and circulation patterns for a major flood in France in 1995, *Water Resources Research*, *49*(10), 6381–6392, 2013.

Machado, M. J., B. A. Botero, J. López, F. Frances, A. Díez-Herrero, and G. Benito, Flood frequency analysis of historical flood data under stationary and non-stationary modelling, *Hydrology and Earth System Sciences*, *19*(6), 2561–2576, 2015.

Maraun, D., T. J. Osborn, and N. P. Gillett, United Kingdom daily precipitation intensity: improved early data, error estimates and an update from 2000 to 2006, *International Journal of Climatology*, 2008.

Mardia, K. V., Measures of Multivariate Skewness and Kurtosis with Applications, *Biometrika*, *57*(3), 519, 1970.

Martins, E. S., and J. R. Stedinger, Generalized maximum-likelihood generalized extreme-value quantile estimators for hydrologic data, *Water Resources Research*, *36*(3), 737–744, 2010.

Massacand, A. C., H. Wernli, and H. C. Davies, Heavy precipitation on the alpine southside: An upper-level precursor, *Geophysical Research Letters*, *25*, 1438, 1998.

Maurer, E. P., A. W. Wood, J. C. Adam, D. P. Lettenmaier, and B. Nijssen, A Long-Term Hydrologically Based Dataset of Land Surface Fluxes and States for the Conterminous United States, *Journal of Climate*, *15(22)*(22), 3237–3251, 2002.

Menne, M. J., I. Durre, R. S. Vose, B. E. Gleason, and T. G. Houston, An Overview of the Global Historical Climatology Network-Daily Database, *Journal of Atmospheric and Oceanic Technology*, *29*(7), 897–910, 2012.

Mesinger, F., et al., North American Regional Reanalysis, *Bull. Amer. Meteor. Soc.*, *87*(3), 343–360, 2006.

Milly, P. C. D., J. Betancourt, M. Falkenmark, R. M. Hirsch, Z. W. Kundzewicz, D. P. Lettenmaier, and R. J. Stouffer, Stationarity Is Dead: Whither Water Management?, *Science*, *319*(5863), 573–574, 2008.

Moody, J. L., The Influence of Meteorology on Precipitation Chemistry at Selected Sites in the Eastern United States, Ph.D. thesis, The University of Michigan, 1986.

Moody, J. L., and J. N. Galloway, Quantifying the relationship between atmospheric transport and the chemical composition of precipitation on Bermuda, *Tellus B*, *40*(5), 1988.

Mullens, E. D., M. Shafer, and J. Hocker, Trends in heavy precipitation inthe southern USA, *Weather*, *68*(12), 311–316, 2013.

Najafi, M. R., and H. Moradkhani, Analysis of runoff extremes using spatial hierarchical Bayesian modeling, *Water Resources Research*, *49*(10), 6656–6670, 2013.

Najafi, M. R., and H. Moradkhani, A hierarchical Bayesian approach for the analysis of climate change impact on runoff extremes, *Hydrological Processes*, *28*(26), 6292–6308, 2014.

Naveau, P., A. Guillou, D. Cooley, and J. Diebolt, Modelling pairwise dependence of maxima in space, *Biometrika*, *96*(1), 1–17, 2009.

Neal, R. A., and I. D. Phillips, Summer daily precipitation variability over the East Anglian region of Great Britain, *International Journal of Climatology*, 2009.

Neal, R. M., Slice sampling, *The annals of statistics*, *31*(3), 705–767, 2003.

Neiman, P. J., L. J. Schick, F. M. Ralph, M. Hughes, and G. A. Wick, Flooding in Western Washington: The Connection to Atmospheric Rivers*, *dx.doi.org*, *12*(6), 1337–1358, 2011.

Newell, R. E., N. E. Newell, Y. Zhu, and C. Scott, Tropospheric rivers? – A pilot study, *Geophysical Research Letters*, *19*(24), 2401–2404, 1992.

Newman, A., K. sampson, M. P. Clark, A. Bock, R. J. Viger, and D Blodgett, A large-sample watershed-scale hydrometeorological dataset for the contiguous USA, 2014.

Newman, A. J., et al., Development of a large-sample watershed-scale hydrometeorological data set for the contiguous USA: data set characteristics and assessment of regional variability in hydrologic model performance, *Hydrology and Earth System Sciences*, *19*(1), 209–223, 2015.

Nychka, D., and N. Saltzman, Design of Air-Quality Monitoring Networks, in *Case Studies in Environmental Statistics*, pp. 51–76, Springer US, New York, NY, 1998.

O'Connell, D. R. H., D. A. Ostenaa, D. R. Levish, and R. E. Klinger, Bayesian flood frequency analysis with paleohydrologic bound data, *Water Resources Research*, *38*(5), 16–1–16–13, 2002.

Ouarda, T. B. M. J., and S. El Adlouni, Bayesian Nonstationary Frequency Analysis of Hydrological Variables1, *Journal of the American Water Resources Association*, *47*(3), 496–505, 2011.

OConnell, D., Fldfrq3 three parameter maximum likelihood flood frequency estimation with optional probability regions using parameter grid integration, *Bureau of Reclamation, Technical Service Center, Denver, Colorado*, 1999.

Padoan, S. A., M. Ribatet, and S. A. Sisson, Likelihood-Based Inference for Max-Stable Processes, *dx.doi.org*, *105*(489), 263–277, 2010.

Pal, I., B. T. Anderson, G. D. Salvucci, and D. J. Gianotti, Shifting seasonality and increasing frequency of precipitation in wet and dry seasons across the U.S., *Geophysical Research Letters*, *40*(15), 4030–4035, 2013.

Palecki, M. A., J. R. Angel, and S. E. Hollinger, Storm Precipitation in the United States. Part I: Meteorological Characteristics, *Journal of Applied Meteorology*, *44*(6), 933–946, 2005.

Pryor, S. C., J. A. Howe, and K. E. Kunkel, How spatially coherent and statistically robust are temporal changes in extreme precipitation in the contiguous USA?, *International Journal of Climatology*, *29*(1), 31–45, 2009.

R Core Team, *R: A Language and Environment for Statistical Computing*, R Foundation for Statistical Computing, Vienna, Austria, 2014.

Ralph, F. M., and M. D. Dettinger, Storms, floods, and the science of atmospheric rivers, *Eos, Transactions American Geophysical Union*, *92*(32), 265–266, 2011.

Read, L. K., and R. M. Vogel, Reliability, return periods, and risk under nonstationarity, *Water Resources Research*, *51*(8), 6381–6398, 2015.

Reale, O., L. Feudale, and B. Turato, Evaporative moisture sources during a sequence of floods in the Mediterranean region, *Geophysical Research Letters*, *28*(10), 2085–2088, 2001.

Reich, B. J., and B. Shaby, A hierarchical max-stable spatial model for extreme precipitation, *The annals of applied statistics*, *6*(4), 1430–1451, 2012.

Reiss, R.-D., and M. Thomas, *Statistical Analysis of Extreme Values: with Applications to Insurance, Finance, Hydrology and Other Fields* , 3rd edition ed., Birkhäuser, 2007.

Renard, B., A Bayesian hierarchical approach to regional frequency analysis, *Water Resources Research*, *47*(W11513), 1–21, 2011.

Renard, B., and U. Lall, Regional frequency analysis conditioned on large-scale atmospheric or oceanic fields, *Water Resources Research*, *50*(12), 9536–9554, 2014.

Renard, B., and M. Lang, Use of a Gaussian copula for multivariate extreme value analysis: Some case studies in hydrology, *Advances in Water Resources*, *30*(4), 897–912, 2007.

Rousseeuw, P. J., Silhouettes: A graphical aid to the interpretation and validation of cluster analysis, *Journal of computational and applied mathematics*, *20*, 53–65, 1987.

Royston, J. P., An Extension of Shapiro and Wilk's W Test for Normality to Large Samples, *Applied Statistics*, *31*(2), 115, 1982.

Rue, H., S. Martino, and N. Chopin, Approximate Bayesian inference for latent Gaussian models by using integrated nested Laplace approximations, *Journal of the Royal Statistical Society: Series B (Statistical Methodology)*, *71*(2), 319–392, 2009.

Saha, S., et al., The NCEP Climate Forecast System Reanalysis, *Journal of the American Statistical Association*, *91*(8), 1015–1057, 2010.

Salas, J. D., and J. Obeysekera, Revisiting the Concepts of Return Period and Risk for Nonstationary Hydrologic Extreme Events, *19*(3), 554–568, 2014.

Sang, H., Composite Likelihood for Extreme Values, in *Extreme Value Modeling and Risk Analysis Methods and Applications*, 2015.

Sang, H., and A. E. Gelfand, Hierarchical modeling for extreme values observed over space and time, *Environmental and Ecological Statistics*, *16*(3), 407–426, 2009a.

Sang, H., and A. E. Gelfand, Hierarchical modeling for extreme values observed over space and time, *Environmental and Ecological Statistics*, *16*(3), 407–426, 2009b.

Sang, H., and A. E. Gelfand, Continuous Spatial Process Models for Spatial Extreme Values, *Journal of Agricultural, Biological, and Environmental Statistics*, *15*(1), 49–65, 2010.

Sankarasubramanian, A., and U. Lall, Flood quantiles in a changing climate: Seasonal forecasts and causal relations, *Water Resources Research*, *39*(5), 1–12, 2003.

Schaefer, M., B. Barker, V. Singh, D. Frevert, et al., Stochastic event flood model (sefm)., *Mathematical models of small watershed hydrology and applications*, pp. 707–748, 2002.

Schlather, M., Models for Stationary Max-Stable Random Fields, *Extremes*, *5*(1), 33–44, 2002.

Schumacher, R. S., and R. H. Johnson, Characteristics of U.S. Extreme Rain Events during 1999–2003, *dx.doi.org*, *21*(1), 69–85, 2010.

Serinaldi, F., and C. G. Kilsby, Stationarity is undead: Uncertainty dominates the distribution of extremes, *77*, 17–36, 2015.

Shang, H., J. Yan, and X. Zhang, El Niño–Southern Oscillation influence on winter maximum daily precipitation in California in a spatial model, *Water Resources Research*, *47*(11), 1–9, 2011.

Smith, R. L., Max-stable processes and spatial extremes, *Unpublished manuscript*, 1990.

Stan Development Team, *RStan: the R interface to Stan, Version 2.7.0*, 2015a.

Stan Development Team, Stan: A C++ Library for Probability and Sampling, Version 2.7.0 , 2015b.

Stein, M. L., Z. Chi, and L. J. Welty, Approximating likelihoods for large spatial data sets, *Journal of the Royal Statistical Society: Series B (Statistical Methodology)*, *66*(2), 275–296, 2004.

Steinschneider, S., and U. Lall, A hierarchical Bayesian regional model for nonstationary precipitation extremes in Northern California conditioned on tropical moisture exports, *Water Resources Research*, *51*(3), 1472–1492, 2015.

Stohl, A., Computation, accuracy and applications of trajectories—A review and bibliography, *Atmospheric Environment*, *32*(6), 947–966, 1998.

Stohl, A., and P. Seibert, Accuracy of trajectories as determined from the conservation of meteorological tracers, *Quarterly Journal of the Royal Meteorological Society*, *124*(549), 1465–1484, 1998.

Stohl, A., and T. Trickl, A textbook example of long-range transport: Simultaneous observation of ozone maxima of stratospheric and North American origin in the free troposphere over Europe, *Journal of Geophysical Research: Atmospheres*, *104*(D23), 30,445–30,462, 1999.

Tan, X., and T. Y. Gan, Nonstationary Analysis of Annual Maximum Streamflow of Canada, *Journal of Climate*, *28*(5), 1788–1805, 2015.

Towler, E., B. Rajagopalan, C. Seidel, and R. S. Summers, Simulating Ensembles of Source Water Quality Using a K-Nearest Neighbor Resampling Approach, *43*(5), 1407–1411, 2009.

Trenberth, K. E., Atmospheric Moisture Residence Times and Cycling: Implications for Rainfall Rates and Climate Change, *Climatic Change*, *39*(4), 667–694, 1998.

USGS, Guidelines for determining flood flow frequency, *Tech. rep.*, United States Geological Survey, 1981.

Vandenberghe, S., N. E. C. Verhoest, C. Onof, and B. De Baets, A comparative copula-based bivariate frequency analysis of observed and simulated storm events: A case study on Bartlett-Lewis modeled rainfall, *Water Resources Research*, *47*(7), 1–16, 2011.

Varin, C., N. Reid, and D. Firth, An overview of composite likelihood methods, *Statist. Sinica*, pp. 5–42, 2011.

Vecchia, V., Estimation and Model Identification of Continuous Spatial Processes , *Journal of the Royal Statististical Society B*, *50*(2), 297–312, 1988.

Villarini, G., J. A. Smith, and G. A. Vecchi, Changing Frequency of Heavy Rainfall over the Central United States, *26*(1), 351–357, 2013.

Warner, M. D., C. F. Mass, and E. P. Salathé Jr., Wintertime Extreme Precipitation Events along the Pacific Northwest Coast: Climatology and Synoptic Evolution, *Monthly Weather Review*, *140*(7), 2021–2043, 2012.

Wigley, T., J. M. Lough, and P. D. Jones, Spatial patterns of precipitation in England and Wales and a revised, homogeneous England and Wales precipitation series, *Journal of Climatology*, 1984.

Wolter, K., and M. S. Timlin, Monitoring ENSO in COADS with a seasonally adjusted principal component index, *Proc of the 17th Climate Diagnostics*, 1993.

Wolter, K., and M. S. Timlin, Measuring the strength of ENSO events: How does 1997/98 rank?, *Weather*, *53*(9), 315–324, 1998.

Xia, Y., et al., Continental-scale water and energy flux analysis and validation for North American Land Data Assimilation System project phase 2 (NLDAS-2): 2. Validation of model-simulated streamflow, *J. Geophys. Res.*, *117*(D3), D03,110, 2012a.

Xia, Y., et al., Continental-scale water and energy flux analysis and validation for the North American Land Data Assimilation System project phase 2 (NLDAS-2): 1. Intercomparison and application of model products, *J. Geophys. Res.*, *117*(D3), D03,109, 2012b.

Yan, H., and H. Moradkhani, A regional Bayesian hierarchical model for flood frequency analysis, *Stochastic Environmental Research and Risk Assessment*, *29*(3), 1019–1036, 2014.

Yonekura, E., and T. M. Hall, A Statistical Model of Tropical Cyclone Tracks in the Western North Pacific with ENSO-Dependent Cyclogenesis, *dx.doi.org*, *50*(8), 1725–1739, 2011.

Yue, S., and P. Rasmussen, Bivariate frequency analysis: discussion of some useful concepts in hydrological application, *Hydrological Processes*, *16*(14), 2881–2898, 2002.

Zhang, Y., J. M. Wallace, and D. S. Battisti, ENSO-like Interdecadal Variability: 1900–93, *Journal of Climate*, *10*(5), 1004–1020, 1997.

Zhu, Y., and R. E. Newell, A Proposed Algorithm for Moisture Fluxes from Atmospheric Rivers, *Monthly Weather Review*, *126*(3), 725–735, 1998.